Nature Communications

https://doi.org/10.1038/s41467-026-69587-7

Article in Press

Multi-modal skin atlas identifies a multicellular immune-stromal community associated with disrupted cornification and specific T cell expansion in atopic dermatitis

Received: 4 August 2025

Accepted: 30 January 2026

Cite this article as: Fiskin, E., Eraslan, G., Alora-Palli, M.B. *et al.* Multi-modal skin atlas identifies a multicellular immune-stromal community associated with disrupted cornification and specific T cell expansion in atopic dermatitis. *Nat Commun* (2026). https://doi.org/10.1038/s41467-026-69587-7

Evgenij Fiskin, Gökcen Eraslan, Maria B. Alora-Palli, Tanvi Jain, Juan Manuel Leyva-Castillo, Sean Kim, Heather Choe, Caleb A. Lareau, Helena Lau, Emily P. Finan, Isabella Teixeira-Soldano, Brenna LaBere, Anne Chu, Brian Woods, Janet Chou, Michal Slyper, Julia Waldman, Sabina Islam, Lynda Schneider, Wanda Phipatanakul, Craig Platt, Orit Rozenblatt-Rosen, Toni M. Delorey, Orr Ashenberg, Jacques Deguine, Gideon P. Smith, Raif S. Geha, Aviv Regev & Ramnik J. Xavier

Multi-modal skin atlas identifies a multicellular immune-stromal community associated with disrupted cornification and specific T cell expansion in atopic dermatitis

Evgenij Fiskin[1]*, Gökcen Eraslan[1]*§, Maria B. Alora-Palli[2]*, Tanvi Jain[1]*, Juan Manuel Leyva-Castillo[3], Sean Kim[4], Heather Choe[4], Caleb A. Lareau[5]§§, Helena Lau[4], Emily P. Finan[1], Isabella Teixeira-Soldano[1], Brenna LaBere[3,6], Anne Chu[3], Brian Woods[3], Janet Chou[3], Michal Slyper[1], Julia Waldman[1], Sabina Islam[7], Lynda Schneider[3], Wanda Phipatanakul[3], Craig Platt[3], Orit Rozenblatt-Rosen[1]§, Toni M. Delorey[1], Orr Ashenberg[1], Jacques Deguine[1], Gideon P. Smith[2], Raif S. Geha[3]‡, Aviv Regev[1,8]‡§, Ramnik Xavier[1,4,9]‡

[1]Klarman Cell Observatory, Broad Institute of Harvard and MIT, Cambridge, MA, USA
[2]Department of Dermatology, Massachusetts General Hospital and Harvard Medical School, Boston, MA, USA
[3]Division of Immunology, Boston Children's Hospital, Harvard Medical School, Boston, MA, USA
[4]Center for Computational and Integrative Biology, Massachusetts General Hospital and Harvard Medical School, Boston, MA, USA
[5]Departments of Pathology, Stanford University, Stanford, CA, USA
[6]Division of Pulmonology, Section of Allergy-Immunology, Phoenix Children's Hospital, Phoenix, AZ, USA
[7]Center for Immunology and Inflammatory Diseases, Division of Rheumatology, Allergy and Immunology, Massachusetts General Hospital, Harvard Medical School, Boston, MA, USA
[8]Howard Hughes Medical Institute, Department of Biology, Massachusetts Institute of Technology, Cambridge, MA, USA
[9]Department of Molecular Biology, Massachusetts General Hospital and Harvard Medical School, Boston, MA, USA

* Contributed equally

‡ To whom correspondence should be addressed: raif.geha@childrens.harvard.edu, aviv.regev.sc@gmail.com, xavier@molbio.mgh.harvard.edu
§ Present address: Genentech, 1 DNA Way, South San Francisco, CA, USA
§§ Present address: Computational and Systems Biology Program, Memorial Sloan Kettering Cancer Center, New York, NY, USA

Abstract

In atopic dermatitis (AD), skin barrier and immune dysfunction result in chronic tissue inflammation, yet our understanding of the tissue ecosystem remains incomplete. Here, we generate a multi-modal census of 280,518 cells from whole skin tissue samples from 17 adults, including 11 AD patients, integrating it with 430,186 cell profiles from four previous studies into a comprehensive human skin cell atlas. Reconstruction of keratinocyte differentiation revealed disrupted cornification in AD associated with signals from an immune and stromal multicellular community – comprising *MMP12*$^{+}$ and migratory dendritic cells (DCs), cycling innate lymphoid cells (ILC), natural killer cells, inflammatory *CCL19*$^{+}$ *IL4I1*$^{+}$ fibroblasts, and clonally expanded *IL13*$^{+}$*IL22*$^{+}$*IL26*$^{+}$ T cells connected by intercellular feedback loops predicted to impact community assembly. Subsets from this community, along with disrupted cornified keratinocytes, were enriched in GWAS, suggesting that dysfunction in this communication network may initiate AD. Our work highlights disease-associated cell subsets and interactions in chronic skin inflammation.

Introduction

Dysregulation of barrier and immune functions in the skin can result in a chronically inflamed tissue ecosystem. Atopic dermatitis (AD) is a prevalent skin inflammatory pathology[1], characterized by immune infiltrates in the upper dermis, epidermal barrier defects[2], and the presence of a core type 2 polarized immune response that can be accompanied by type 22, type 17 and type 1 response signatures[3]. Topical treatment and therapies targeting the type 2 response, such as antagonistic IL4RA antibodies, are effective in only ~60% of AD patients[4] and have to be given continuously[5], highlighting the unmet need to identify distinct subtypes of the disease and suitable interventions.

Despite extensive studies into the genetic and molecular features of the complex interplay between barrier dysfunction and immune activation in AD pathogenesis[6], many features remain only partly understood. These include aberrant barrier function and terminal keratinocyte differentiation of cornified keratinocytes, cell-cell interactions between keratinocytes and immune cells associated with pathological inflammation, and the precise states of disease-promoting T cells, their TCR clonotype composition and antigen specificity, and associations with other cell types.

Single cell RNA-seq (scRNA-seq) has been instrumental in defining the cellular landscape in human health and disease[7], providing crucial insights into homeostasis and pathology in different tissues, including the healthy and inflamed human skin. Atopic dermatitis scRNA-seq studies have provided an initial cell census and nominated disease-related cells, but have been limited to either small patient cohorts[8–10] ($n \leq 5$), low cell recovery per patient, gene expression profiles without TCR clonotype information, or specific cell or tissue sub-compartments[11–18]. Thus, our understanding of the skin cellular ecosystem and its remodeling upon inflammation remains

incomplete.

Here, we generated a large-scale, high resolution, multi-modal single cell atlas of RNA and TCR clonotype profiles in healthy and inflamed human skin. We collected 280,518 scRNA-seq profiles from 27 samples from 17 individuals, including non-lesional and lesional skin from 11 AD patients with mild to severe disease. For comparison to AD, we also collected four samples from two individuals with scleroderma, totaling 29,689 cells. We combined our collected dataset with 430,186 cells from four re-annotated public skin scRNA-seq datasets[8,10–12] into an integrated atlas of 710,704 cells, along with deconvoluted bulk RNA-seq profiles from an additional cohort of 27 AD patients[19]. We annotated 86 cell subsets, including multiple previously unknown and disease-specific cellular subsets. Computational inference of the keratinocyte (KC) differentiation trajectory from basal to cornified layers revealed disruption in AD of the normal cornification process. Joint scRNA-seq and T cell receptor (TCR) sequencing of lesional skin T cells identified a unique, clonally expanded, T cell state with overlapping type 2 and type 17 characteristics that co-expresses the key cytokines *IL13*, *IL22* and *IL26*. Both cornified keratinocytes and *IL13*$^{+}$*IL22*$^{+}$*IL26*$^{+}$ T cells were enriched for atopic dermatitis risk genes nominated by GWAS. In AD, a DC activation trajectory was shifted towards a unique mature migratory DC (mmDC) state, predicted to promote the pathological T cell response. Furthermore, mmDCs and *IL13*$^{+}$*IL22*$^{+}$*IL26*$^{+}$ T cells, along with lesion-specific stromal cell subsets and select neuronal subsets, formed a multicellular community through multiple inter-cellular positive feedback loops, generating signals that can impact aberrant KC differentiation and skin pathology in AD.

Results

An integrated, multi-modal human single-cell atlas of healthy and AD skin

To construct a multi-modal cell atlas of healthy, AD non-lesional, and AD lesional adult human skin, we analyzed 27 samples from a cohort of 17 adult individuals, including 21 samples (11 from lesional skin, 10 from non-lesional skin) from 11 AD patients and one sample from each of 6 sex-matched healthy control subjects, spanning Caucasian, Black, Asian and Hispanic descent (**Fig. 1a** and **Supplementary Fig. 1**). For comparison to AD, we also collected four samples from two patients with scleroderma (**Fig. 1a**). Unlike some prior work[10–12], we profiled the entire tissue without flow enrichment by establishing a tissue dissociation workflow of whole 3 mm skin punch biopsies into single cell suspensions. We analyzed cells using droplet-based 3'-scRNA-seq and 5'-scRNA-seq with scTCR-seq (**Fig. 1a, Methods**). We retained 280,518 high-quality 3'-scRNA-seq profiles from 39 channels (7 healthy and 32 AD), 29,689 high-quality 3'-scRNA-seq profiles from scleroderma samples, and 7,256 T cells with 5'-scRNA-seq, and assigned TCR sequences (clones) for eight AD patients within our cohort (**Fig. 1a** and **Supplementary Fig. 1, 2a-c**; **Methods**). There was reasonable sample mixing across individuals within each cell subset even without correcting for batch effects (**Fig. 1g** and **Supplementary Fig. 2d**), allowing for downstream analysis without batch correction.

Iterative clustering and *post hoc* annotation (**Methods**) resolved 16 broad cell categories (**Fig. 1b** and **Supplementary Fig. 2e**) and 86 granular cell subsets (**Fig. 1c,d** and **Supplementary Fig. 3a; Supplementary Dataset 1**), including some reflecting previously-unidentified states and rare cells. These included, for example, *MMP12*$^+$ DCs, *CPE*$^+$ fibroblasts, *NGFR*$^+$ and *CDH19*$^+$ Schwann-like fibroblasts that are *CD90/THY1*-negative, multiple rare skin appendageal cell subsets (containing hair follicles, sweat gland and sebaceous gland subsets), and cycling innate lymphoid cells (ILCs) (**Supplementary Fig. 3a-e**). As expected, KC expression of key epidermal

inflammatory markers *S100A8* (FDR - $1.04*10^{-7}$, Wald test; **Methods**) and *KRT16* (FDR - $1.01*10^{-8}$, Wald test) was much higher in lesional (inflamed) vs. non-lesional or healthy samples (**Fig. 1e,f** and **Supplementary Fig. 3f,g**).

To corroborate the cell subsets and generate a cross-study skin cell atlas, we built a linear classifier based on the 86 granular cell subsets. We then classified profiles from four previous scRNA-seq studies of healthy and AD skin[8,10–12] and co-embedded these re-annotated cell profiles with our data for an integrated skin cell atlas of 710,704 cell profiles (**Supplementary Fig. 4a-g**; **Methods; Supplementary Dataset 5**). Overall, cell type annotations and composition were coherent between prior datasets and our study (**Supplementary Fig. 4a-g; Supplementary Dataset 6**), suggesting that the atlas is robust and comprehensive, although some of the fine cell subsets we identified were not captured in previous data (**Supplementary Fig. 4h-j**). Most strikingly, our atlas included cornified keratinocytes and select dermal stromal subsets that may be absent from prior studies, as they are either difficult to capture (cornified keratinocytes) or underrepresented in suction blistering, which mainly captures the epidermis (dermal subsets)[11,12] (**Supplementary Fig. 4h-j**).

Increased DCs, T cells and NK cells in AD skin

Comparison of the overall cellular composition between healthy, non-lesional and lesional AD skin in our dataset revealed an increased proportion of DCs in both non-lesional (FDR - 0.0336, Multinomial Dirichlet regression, **Methods)** and lesional (FDR - $2.50*10^{-8}$) AD skin compared to healthy skin, as well as of T and natural killer (NK) cells (FDR - 0.0793), macrophages (FDR - 0.0646) and neutrophils (FDR - 0.0178) in lesional skin (**Fig. 1g,h** and **Supplementary Fig. 5; Supplementary Dataset 2**), consistent with infiltration of immune cells into lesions[1]. Conversely,

there was a reduced proportion of pericytes/smooth muscle cells (SMCs) in non-lesional (FDR - 0.0274) and lesional (FDR - $1.17*10^{-9}$) AD skin, and of vascular endothelial cells (FDR - $4.95*10^{-8}$), melanocytes (FDR - $4.34*10^{-3}$) and sweat gland cells (FDR - $1.32*10^{-6}$) in lesional skin (**Fig. 1g,h** and **Supplementary Fig. 5; Supplementary Dataset 2**).

Comprehensive reconstruction of keratinocyte differentiation

Skin barrier formation is accomplished via terminal differentiation of KCs through basal, suprabasal, spinous, granular and cornified layers[20,21]. Graph-based clustering and partition-based approximate graph abstraction (PAGA)[22] of KCs (**Methods**) revealed 8 interconnected KC states that recapitulated known features of KC differentiation (**Fig. 2a**): from basal marker-expressing KC1s (*KRT15*, *COL17A1*) towards cycling KC (*UBE2C*, *TOP2A*) and KC2s (*MT1X*, *MT1G*), spinous marker-positive KC3s (*KRT1*, *KRT10*), granular marker-expressing KC4s (*KRT2*, *DSC1*) and KC5s (*CNFN*, *KLK7*), and finally cornified KC1s (*SPRR2A*, *SPRR2B*) and cornified KC2s (*IL37*, *PSORS1C2*, *LCE1B*) (**Fig. 2a-c** and **Supplementary Fig. 6a-c; Supplementary Dataset 1**), with gene sets enriched in the different KC subsets consistent with known biology (**Supplementary Fig. 6f; Methods; Supplementary Dataset 3**). Several lines of evidence support the ordering from KC5 to cornified KC1 and KC2s, including differential expression of late cornified envelope (*LCE) vs*. basal and spinous KC marker genes (**Supplementary Fig. 6d**), higher expression of autophagy and mitophagy genes in cornified KCs (**Supplementary Fig. 6f**)[23], and RNA velocity analysis[24,25] (**Supplementary Fig. 6e**).

Next, reconstructing healthy human KC differentiation as a continuous process (by calculating diffusion pseudotime (DPT)[26] for KCs from all healthy samples; **Methods**), we observed a

consistent ordering, and captured dynamic gene expression changes along differentiation (**Fig. 2d; Methods**), aligned with the spatial localization of corresponding marker proteins in Human Protein Atlas (**Fig. 2e**). This highlighted the temporal patterns of key known differentiation transcription factors (TFs) (*TP63, GATA3, GRHL3, GRHL1, PRDM1*)[27–29] and TFs not previously associated with differentiation (*e.g., NFE2, NPAS1, ETV7*) (**Supplementary Fig. 6g,h**), as well as monogenic skin disease genes. For example, expression of epidermolysis bullosa-causing genes peaked at early DPT points in basal KCs, whereas ichthyosis-causing genes peaked at late DPT points in upper granular and cornified layers (**Supplementary Fig. 6i**), in line with roles in KC attachment to the basement membrane and lipid cornified envelope formation, respectively.

Altered keratinocyte differentiation and cornified layer in lesional AD skin

Skin inflammation in AD altered the KC trajectory and KC states, with remodeling of the cornified KC layer and a shift from cornified KC2 towards cornified KC1. First, there was an increase in the fraction of cycling KCs (FDR - $2.01*10^{-3}$, Multinomial Dirichlet regression) and granular KC4s (FDR - $1.92*10^{-6}$) in lesional AD skin, and a decrease in basal KC1s (FDR - $3.3*10^{-3}$**Fig. 2f,g** and **Supplementary Fig. 7a; Supplementary Dataset 2**), and a shift from cornified KC2s dominant in healthy samples (FDR - 0.0279 to near-exclusive cornified KC1s in AD lesional skin (FDR - 0.0786) (**Fig. 2h,i** and **Supplementary Fig. 7b; Supplementary Dataset 1**). This was related to an altered KC differentiation trajectory in lesional AD compared to healthy or non-lesional skin based on diffusion pseudotime (DPT, **Fig. 2j**; **Methods**). Lesional KC5s had a significantly later DPT, with one particularly delayed mode, and lesional cornified KCs (cKCs) were primarily cKC1s, with an earlier DPT mode (**Fig. 2h,j**; FDR - $5.71*10^{-11}$ and $7.28*10^{-17}$ respectively, Mann–Whitney U test). This suggests a model where lesional AD is characterized by

a shift from basal KC1s to cycling KCs, followed by decreased differentiation from KC5s to cKCs, leading to defective cornification. This shift was accompanied by decreased cell-intrinsic expression of late cornified envelope genes in lesional AD KCs (*e.g.*, *LCE5A*, *LOR*) and an increase in small proline-rich proteins (*SPRR* genes) (**Fig. 2k; Supplementary Dataset 4**), also captured by bulk RNA-Seq[19] (**Supplementary Fig. 7c**). Remodeling of the cornified KC layer and the shift away from cornified KC2 and concomitant increase in cornified KC1 were not observed in non-lesional AD skin and lesional samples from two scleroderma patients (**Supplementary Fig. 7f,g**), emphasizing unique lesional AD-driven alterations to cornification. Future studies will be required to conclusively determine whether this observed altered keratinocyte differentiation results from an arrest in differentiation or from changes in cell state and survival across different layers of the AD skin.

There was also increased cell-intrinsic expression in lesional KCs of epidermal inflammatory markers, interferon pathway genes, antimicrobial response genes, lipid and rate-limiting cholesterol metabolism genes (**Fig. 2k** and **Supplementary Fig. 7d; Supplementary Dataset 3**)[8,10,13], and IL-20-related cytokine genes *IL19* and *IL24* (**Supplementary Fig. 7e**), implicated in epidermal hyperplasia and barrier dysfunction in AD[30]. Across all KCs, cornified KCs preferentially expressed IL-1 family cytokines and regulators (*IL1A, IL1B, IL18, IL36G, IL37, IL1F10/IL38, IL36RN*) and inflammasome pathway-related genes (*GSDMA, NLRP10, PYDC1*) (**Fig. 2l** and **Supplementary Fig. 7d**), consistent with prior *in vitro* observations[31]. While pro-inflammatory *IL36G* was up-regulated in lesional cornified KCs (FDR < 10^{-16}, Wald test), anti-inflammatory cytokines *IL37* and *IL1F10/IL38* were down-regulated (FDR < 10^{-16} and FDR = $3.39*10^{-6}$).

ScRNA-seq of dissociated dorsal skin from control and MC903-treated mice, a model of AD-like skin inflammation[32], mirrored many aspects of human epidermal inflammation (**Supplementary Fig. 8a-d, Methods**), consistent with previous work[33]. Analogous to human AD, MC903-treated inflamed skin displayed a loss of cornified KCs (**Supplementary Fig. 8f,g**), increased antimicrobial peptides and *Sprrs*, decreased levels of *Lce* genes and increased cycling KCs (**Supplementary Fig. 8h**,**i**). However, unlike in human AD, *Il4*$^+$/*Il13*$^+$ basophils arose in MC903-treated skin (**Supplementary Fig. 8g,j**), as another source of type 2 cytokines (**Supplementary Fig. 8j**), consistent with reports of *Il4*$^+$ basophils as essential drivers of pathology in the MC903 model[34]. Increased numbers of *Il4*$^+$/*Il13*$^+$ basophils as well as decreased expression of cornification genes have been noted in the murine OVA sensitization model of AD-like skin inflammation, indicating that observed changes are congruent across various mouse AD disease models[35].

Two DC maturation trajectories in healthy, non-lesional and lesional skin

Myeloid cells from healthy and AD skin spanned a continuum of cell states, which we broadly partitioned into multiple *C1QA*-high macrophage (MΦ) subsets (*C1QA, MS4A7, MAF, CCL18, CCL13*), inflammatory *IL1B*$^+$ MΦ (*IL1B, MMP9*), lipid-associated *SPP1*$^+$ MΦ (*SPP1, LPL*)[36], tissue-resident Langerhans dendritic cells (LDCs) (*CD207/Langerin, FCGBP*), DC1s (*CLEC9A, XCR1*) and DC2s (*CD1C, FCER1A*)[37], *CD83*$^+$ DC2s, inflammatory *IL1B*$^+$ DCs (previously coined DC3s[38]; *IL1B, IL23A, CXCL8*), recently identified *MMP12*$^+$ DCs (*MMP12, CD1B, RAB7B*), mature migratory DCs (mmDCs) (*LAMP3, CCR7*; also referred to as mature DCs enriched in immunoregulatory molecules (mregDCs)[39]), cycling DC1s and DC2s (*UBE2C, MKI67*), as well as neutrophils (*CXCL8, FCGR3B, S100P*) (**Fig. 3a,b** and **Supplementary Fig. 9a;**

Supplementary Dataset 1).

In DCs we inferred two distinct maturation trajectories, both originating from DC2s and transitioning either through *MMP12*$^{+}$ DCs towards mmDCs (Trajectory 1) or via *CD83*$^{+}$ DC2s towards inflammatory *IL1B*$^{+}$ DCs (Trajectory 2) (**Fig. 3c-e** and **Supplementary Fig. 9b-d**). Additional paths involving Langerhans cells are also suggested in the model, but were not fully resolved (**Fig. 3c**).

Within trajectory 1, *MMP12*$^{+}$ DCs constituted a *CD40*^{hi}*CD83*^{hi}*CD86*^{lo}*LAMP3*^{lo}*CCR7*^{lo} transition state, suggesting an activated, but non-fully mature DC state (**Fig. 3d** and **Supplementary Fig. 9d**) preceding mmDCs. Consistent with DC activation, *MMP12*$^{+}$ DCs highly expressed antigen presentation genes (*HLA-DRB1, HLA-DQB1, CD1B, CD1A*), maturation-controlling TFs (*REL, NFKB1, SPI1, IRF4*) and co-stimulatory membrane proteins (*CD226, CD40, CD83, TNFRSF4/OX40*) (**Fig. 3d** and **Supplementary Fig. 9d**). Apart from expressing the key AD disease marker gene *MMP12*[40], these *MMP12*$^{+}$ DCs also expressed genes encoding select protease inhibitors (*CST6, CST7*) and Langerhans cell markers (*CLDN1, CD207/Langerin*) (**Fig. 3d** and **Supplementary Fig. 9b**), indicating the presence of activated LDCs among *MMP12*$^{+}$ DCs. Along trajectory 1, *MMP12*$^{+}$ DCs progressed towards mmDCs, which expressed reported mregDC signatures[39,41,42], including the key TF *IRF4*[43], actin cytoskeleton and migration genes, DC maturation markers, an immunomodulatory program (*CD274/PD-L1, PDCD1LG2/PD-L2, CD200, IDO1*)[8,10–12,39], *CCL22* and *CCL17,* AD disease markers involved in recruitment of *CCR4*$^{+}$ type 2 inflammatory T cells[44], TSLP alarmin receptor (*CRLF2, IL7R*)[12], and the cytokines *IL15* and IL27 subunit *EBI3* (**Fig. 3d** and **Supplementary Fig. 9d**), as noted previously[8,10–12,39].

MmDCs profiles had striking similarities to mouse *IRF4*$^{+}$ PD-L2^{+} mature DCs (**Supplementary Fig. 9e**), which are essential regulators of type 2 immunity to protease allergen and worm infection[43,45].

In trajectory 2, DC2s transitioned via a *CLEC10A*^{hi} *FCER1A*^{hi} *CD83*$^{+}$ transition state (*CD83*$^{+}$ DC2s) towards *IL1B*$^{+}$ DCs, which were characterized by high expression of distinct TFs (*CEBPB, HIF1A, STAT3*), select chemokines (*CXCL2, CXCL3, CXCL8*), DC maturation markers (*CCR7, LAMP3*) and abundant expression of *IL1B* and psoriasis-associated *IL23A* (**Fig. 3e, Supplementary Fig. 9e**), an expression signature consistent with reported skin DC3s[38]. The two sets of TFs highlighted in the two trajectories are part of a mutually exclusive gene circuit previously described in bone marrow derived mouse DCs (**Supplementary Fig. 9e**)[46].

Enhanced differentiation leads to enriched mmDCs in AD

Across DCs, both *MMP12*$^{+}$ DCs and mmDCs were highly increased in lesional skin (FDR - $3.75*10^{-6}$, Multinomial Dirichlet regression and FDR - $1.65*10^{-7}$, respectively), with *MMP12*$^{+}$ DCs also enriched in non-lesional channels compared to healthy controls (FDR - $3.47*10^{-5}$) (**Fig. 3f; Supplementary Dataset 2**), while the proportion of DC *IL1B*$^{+}$ and *CD83*$^{+}$ DC2s was unchanged (**Fig. 3f** and **Supplementary Fig. 9f**,**g**). The fractions of *MMP12*$^{+}$ DCs and mmDCs were also increased in non-lesional and lesional skin in scRNA-seq from two other AD patient cohorts annotated by our classifier[8,11] (**Supplementary Fig. 9h,i**; **Supplementary Dataset 5; Methods**) and when deconvolving bulk RNA-seq from AD patients[19] (**Fig. 3g** and **Supplementary Fig. 9j**; **Methods**). *MMP12*$^{+}$ DCs and mmDCs in lesional skin had increased predicted *STAT6* TF activity (**Supplementary Fig. 9k; Supplementary Dataset 7; Methods**),

which could impact mmDC activation or differentiation, as seen for IL4-driven PD-L2^{+} mature DCs in mice[43].

Comparing differentiation pseudotimes for Trajectory 1 shows a shift in differentiation between healthy, non-lesional and lesional DCs. Lesional mmDCs had a later DPT compared to healthy and non-lesional counterparts (Kolmogorov–Smirnov (KS) test; FDR - 0.0625 and FDR - 4.55*10^{-5}, respectively), while non-lesional *MMP12*$^{+}$ DCs had a later DPT compared to healthy and lesional cells (FDR - 0.0120and FDR - 8.88*10^{-16}) (**Supplementary Fig. 9l**). Along with the increased fraction of *MMP12*$^{+}$ DCs and mmDCs in lesional skin, this is consistent with a model where a partially activated state arises in non-lesional *MMP12*$^{+}$ DCs that becomes a fully activated mmDC state in lesional AD.

As mmDCs/mregDCs were reported in various inflammatory diseases[39,41,42,47], we compared the distinguishing features of mmDCs in AD to the human mmDC/mregDC landscape. We assembled a human mmDC atlas of 2,551 mmDCs expressing our core mmDC signature from 24 scRNA-seq datasets across tissues and diseases, including 1,025 AD mmDCs from our study (**Fig. 3h,i; Methods; Supplementary Datasets 5 and 8**). Compared to other mmDCs, those from lesional AD skin constitute a *CCL22*^{hi} *CCL17*^{hi} *CCL19*^{lo} *IDO1*^{lo} state (**Fig. 3j,k, Supplementary Fig. 9m,n, Supplementary Dataset 9**), consistent with a function in polarizing towards a type 2 immune response.

A T cell inflammatory program including *IL13*, *IL22* and *IL26* is active in CD4 and CD8 T cells in skin

The 16 lymphocyte subsets included *CD3D*-negative NK cells (*KLRD1, KLRF1, GNLY*^{hi}) and ILCs (*KIT, MB, SPINK2*), γδT cells *(TRGC2, FXYD2, ZNF683/HOBIT)*, *CD8A*$^{+}$ cytotoxic T cells (*CD8A, CCL5, GZMK*), CD4^{+} regulatory T cells (T_{regs}) (*CTLA4*, *TIGIT*, *FOXP3*, *CCR8*), multiple *CD40LG*$^{+}$ T cells with T *CREM*^{hi} (CREM, *CXCR4*) and T *FOS*^{hi} (*FOS*, *IL32*) states in both CD4^{+} and CD8^{+} T cells, naive/memory B cells (*MS4A1/CD20, CD79A, SELL/CD62L*), and plasmablasts (*FKBP4, IRF8*) and IgA or IgG-expressing plasma cells (*JCHAIN*, *MZB1*, *TNFRSF17*) (**Fig. 4a,b** and **Supplementary Fig. 10a-e; Supplementary Dataset 1**).

Because many skin lymphocytes vary continuously — rather than in discrete subsets — and can share cellular processes[48], we characterized lymphocyte gene programs in healthy, non-lesional, and lesional skin samples using stochastic block modeling (SBM)[49], a hierarchical topic modeling approach (**Methods**). While some programs reflected distinct cell types, such as regulatory (topic #148) and cytotoxic (#227) T cells (**Supplementary Fig. 10f; Supplementary Dataset 10**), others reflected cell biological processes (cell cycle, #97), or key immune processes (#196).

A prominent inflammatory immune program (#190) was expressed across multiple T cell subsets (**Fig. 4c,d**), and included key type 2 or 17 genes, such as cytokines *IL13, IL5*, pruritogenic *IL31*, *IL22* and *IL26, IL25* alarmin receptor *IL17RB* and arachidonic acid, prostaglandin, and eicosanoid pathway genes (*TBXAS1, HPGDS, PTGDR2* (*CRTH2*), *SLC27A2, ALOX5AP*, *PLA2G16*) (**Fig. 4e** and **Supplementary Fig. 10g,h**; **Methods**), including *PPARG*, which has been implicated in Th2 cell differentiation and activation[50,51]. *IL31* expression may allow interaction with dorsal root ganglia (DRG) NP3 neurons expressing *IL31* receptor subunits (*IL31RA, OSMR*), based on scRNA-seq of 2,518 non-human primate DRG neurons[52] (**Supplementary Fig. 13f-h**; **Methods**). Both CD4^{+} and CD8^{+} T cells expressed this program, most prominently *CREM* and *FOS*^{hi} T cells

(log OR=1.269, p-value (of positive association) $1.28x10^{-167}$, Fisher's exact test), whereas T_{regs} and *CD8*$^{+}$*GZMK*$^{+}$ cytotoxic lymphocytes mostly did not (log OR=-1.883, p-value (of negative association) $9.8x10^{-85}$, Fisher's exact test, **Supplementary Fig. 10i**,**j**), as expected for an inflammatory effector program.

A shift from cytotoxic to pro-inflammatory *IL13*/*IL22*/*IL26* expressing T cell clones in lesional AD skin

In contrast to a largely *CD8*$^{+}$ cytotoxic T cell compartment in healthy skin, lesional AD had a higher proportion of *CD4*$^{+}$ T cells (p-value - 0.0105, Dirichlet regression), as previously described[53] (**Fig. 4f**). Lesional AD also had an increased fraction of non-cycling and cycling T_{regs} (FDR - $3.97*10^{-3}$, Multinomial Dirichlet regression and FDR - $1.24*10^{-8}$), cycling *FOS*^{hi} T cells (FDR - $3.27*10^{-9}$), cycling ILCs (FDR - $4.72*10^{-3}$) and *IgG*$^{+}$ plasma cells (FDR - $2.71*10^{-3}$) (**Fig. 4g** and **Supplementary Fig. 10k; Supplementary Dataset 2**). Cycling ILCs in lesional skin expressed cytotoxic genes (*GZMB, KLRC1, PRF1*), *CCL1*, and key inflammatory mediators *CSF2/GM-CSF*, the OX40 ligand *TNFSF4*[54], and the cytotoxicity and tissue-residency TF *ZNF683/HOBIT*[55,56] (**Fig. 4h**). T_{regs} in lesional skin expressed higher levels of *TNFRSF9* (4-1BB), *TNFRSF4* (OX40), *TNFRSF18* (GITR) and T cell activation markers (*CD69, HLA-DPA1*) (**Fig. 4i; Supplementary Dataset 4**).

To find AD-specific programs, we calculated differential topic expression between lesional and healthy skin samples and identified topic 190 ($6.33*10^{-143}$, Multinomial Dirichlet regression), with T cells expressing an inflammatory immune program, as the most differentially expressed topic (**Fig. 4j,k)**. This is in line with an AD-specific shift from cytotoxic to pro-inflammatory T cell states. We also identified significant changes in Treg (#148), cell cycle (#111, #97, #94, #23) and

T cell activation/differentiation programs (#53, #113, #196) (**Fig. 4j,k** and **Supplementary Fig. 10f**; **Supplementary Dataset 10**), and a decrease in cytotoxic programs (#227, #78) (**Fig. 4j,k** and **Supplementary Fig. 10f**; **Supplementary Dataset 10**). Consistently, an increased fraction of cells expressed *IL13*, *IL22*, and *IL26* in both non-lesional and lesional AD skin (FDR<5%, Mann-Whitney U test) and a smaller fraction expressed *IFNG* in lesional AD *vs*. healthy channels (**Fig. 4k** and **Supplementary Fig. 10l**)[8,12]. In lesional skin, T cells expressing two or three of *IL13*, *IL22* and *IL26* emerged, especially among cycling FOS^{hi} T cells, such that most (>66%) $IL13^{+}$ cells also co-expressed at least one of *IL22* and *IL26* (**Fig. 4l,m**).

Combined scTCR-seq and 5'-scRNA-seq of lesional biopsies from eight patients (**Fig. 4n and Supplementary Fig. 10m; Supplementary Dataset 11; Methods**) detected 2,294 expanded ($n \geq 2$ T cells with shared TCR) and 3,753 non-expanded ($n = 1$ T cell with a given TCR) $CD4^{+}$ T cells (**Fig. 4o** and **Supplementary Fig. 10n,o**), with strong enrichment of *IL13/IL22/IL26* double- and triple-positive T cells and topic 190 expression in expanded vs. non-expanded $CD4^{+}$ T cells (**Fig. 4p-s** and **Supplementary Fig. 10p-q; Supplementary Dataset 12**). This suggests the presence of a disease-associated, clonally expanded, pro-inflammatory T cell population with overlapping type 2 and type 17 characteristics.

Remodeling of the AD stroma with increase in immunoregulatory fibroblasts

Stromal cells in skin spanned eleven subsets of fibroblasts, eight subsets of vascular and lymphatic endothelial cells (**Fig. 5a-c,**), as well as 5 pericyte subsets (**Supplementary Fig. 11a,b**), smooth muscle cells, and myelinating and non-myelinating Schwann cells (**Table S1**). The eleven fibroblasts subsets (**Fig. 5d,e** and **Supplementary Fig. 11c,d**) included two subsets of $CCL19^{+}$ fibroblasts enriched for immune regulating functions: $CCL19^{+}IL4I1^{+}$ fibroblasts (*IL32*, *TNC*,

VCAM1) expressing high levels of MHC-I and II presentation genes (**Fig. 5f** and **Supplementary Fig. 11e**) and *CCL19*$^{+}$*APOE*$^{+}$ fibroblasts (*RBP5, TNFRSF13B, CXCL1*) (**Supplementary Fig. 11e**), both expressing markers previously reported in *CCL19*$^{+}$ and *ADAMDEC1*$^{+}$ fibroblasts in other human pathologies, including ulcerative colitis[57,58]. Fibroblasts also included two subsets expressing markers of recently described nerve-associated fibroblasts[59]: *CDH19*$^{+}$ cells (*SCN7A, ANGPTL7, EBF2*) and *NGFR*$^{+}$ cells (*ITGA6, TNNC1, WNT6*) (**Fig. 5d,e** and **Supplementary Fig. 11f,g**). In addition to recently-reported *THY1*$^{+}$ skin stromal cells[15], our sorting-free workflow revealed multiple *THY1*$^{-}$ stromal cell populations, including *CDH19*$^{+}$ and *NGFR*$^{+}$ cells and *RERGL*$^{+}$ and *DES*$^{+}$ smooth muscle cells.

Stromal subset composition changed substantially in AD lesions vs. healthy skin, with significantly higher fractions of *CCL19*$^{+}$*IL4I1*$^{+}$ fibroblasts (FDR - $2.12*10^{-6}$, Multinomial Dirichlet regression), *GDF10*$^{+}$ fibroblasts (FDR - $7.18*10^{-4}$), *INSR*$^{+}$ CapEC (FDR - $5.00*10^{-3}$) and *ICAM2*^{hi} ArtEC (FDR - 0.0106) and lower proportion of papillary fibroblasts (FDR - $3.96*10^{-4}$) and *EDNRB*^{hi} CapECs (FDR - $6.91*10^{-3}$) (**Fig. 5g** and **Supplementary Fig. 11h-j; Supplementary Table 2**). Consistent with a recent report[8], *CCL19*$^{+}$*IL4I1*$^{+}$ fibroblasts showed the most pronounced increase in AD lesions, which we further confirmed in re-annotated published AD single-cell[8,11] and deconvoluted bulk RNA-seq[19] (**Fig. 5g** and **Supplementary Fig. 11k**). Compared to counterparts in healthy skin, *CCL19*$^{+}$*IL4I1*$^{+}$ fibroblasts in lesional skin had increased expression of type VI collagen genes, *PDPN*, the *IL13* decoy receptor *IL13RA2*, T cell and neutrophil recruiting chemokines (*CCL19, CXCL1*) and regulators of immune cell adhesion and tissue repair (*VCAM1, POSTN*) (**Fig. 5h; Supplementary Table 4**). These are similar to features of *CCL19*$^{+}$ fibroblasts in the colon in inflammatory bowel disease[58] and in tertiary lymphoid

structures of salivary glands[60].

A multicellular community of mmDCs, *IL13*$^+$/*IL22*$^+$/*IL26*$^+$ T cells, NK cells, cycling ILCs and *CCL19*$^+$*IL4I1*$^+$ fibroblasts in AD may impact KC differentiation

Healthy, non-lesional, and lesional channels separated by their cellular composition (**Fig. 6a** and **Supplementary Fig. 12a-g**) in a Principal Component Analysis (PCA), with the second principal component (PC2) capturing variation between lesional and non-lesional/healthy channels, reflecting the joint increased presence of *IL13*$^+$/*IL22*$^+$/*IL26*$^+$ T cells, mmDCs, *MMP12*$^+$ DCs, neutrophils and *CCL19*$^+$*IL4I1*$^+$ fibroblasts and the strong depletion of cornified KC2 in lesions (**Fig. 6b**). PC2 captured further heterogeneity between patient channels, distinguishing those with higher fractions of neutrophils and *IL1B*$^+$ DCs (**Supplementary Fig. 12d**), consistent with increased neutrophil numbers observed in AD patients[61] (**Fig. 1h**).

Cell fractions of lesion-enriched immune and stromal cell subsets were highly correlated with each other across samples, identifying several multicellular communities in lesional skin (**Fig. 6c** and **Supplementary Fig. 12h,i**), including one community comprising *IL13*$^+$/*IL22*$^+$/*IL26*$^+$ T cells, cycling *FOS*^{hi} T cells, mmDCs, *MMP12*$^+$ DCs and *CCL19*$^+$*IL4I1*$^+$ fibroblasts (community 1) (**Fig. 6c** and **Supplementary Fig. 12h,i**), and another (partly overlapping) with neutrophils, *IL1B*$^+$ DCs and *CREM*^{hi} T cell subsets (community 2) (**Supplementary Fig. 12h,i**). We further validated the presence and structure of these communities using public AD spatial datasets. First, RNA in situ hybridization demonstrated that T cells are the main source of *IL13* in AD lesional skin[62]. Second, spatial transcriptomics (10x Visium) of AD lesional skin identified neighboring cells (55 μm tissue spots) with a distinct transcriptional signature of *IL13*, *IL13RA1*, *IL13RA2*, *CCL17*, *CCL19*,

CCL22, and *MMP12*[63], matching community 1 members in our AD atlas including *IL13*$^{+}$/*IL22*$^{+}$/*IL26*$^{+}$ T cells, cycling *FOS*^{hi} T cells, *CCL19*$^{+}$*IL41*$^{+}$ fibroblasts, mmDCs, and *MMP12*$^{+}$ DCs (**Fig. 6d,e**). Similarly, we observed a separate set of spatially neighboring cells expressing *IL17A*, *CXCL1*, *CXCL8*, *CCL20*, *IL22*, and *IL26*[63], matching community 2 members including *IL1B*$^{+}$ DCs and *IL13*$^{+}$/*IL22*$^{+}$/*IL26*$^{+}$ T cells (**Supplementary Fig. 12h, 13c**).

Community 1 was supported by multiple intra-community receptor-ligand (R-L) interactions that are significantly enriched in lesional AD (**Fig. 6d-f** and **Supplementary Fig. 13a**; **Methods; Supplementary Dataset 13**), with multiple self-reinforcing positive feedback loops that may contribute to community assembly and stability, especially between *FOS*^{hi} T cells, mmDCs, ILCs, and *CCL19*$^{+}$*IL41*$^{+}$ fibroblasts (**Fig. 6f**). For example, mmDCs expressed *CCL19*, *CCL17*, and *IL15*, which recruit and expand T cells and ILC/NK cells, respectively[64], and, in turn, cycling *FOS*^{hi} T cells expressed *TNFSF4*, *FLT3LG*, *CSF2* and *TNFSF11/RANKL*, which are mediators of DC activation, expansion, survival and maturation[65–67] (**Fig. 6d-f** and **Supplementary Fig. 13a**). Consistent with this model, there was a positive correlation between the level of *CCL19* and *CCL17* cell intrinsic expression in mmDCs and the proportion of cycling *FOS*^{hi} T cells (**Fig. 6f** and **Supplementary Fig. 13e**; Spearman's $\rho = 0.84$ and 0.76; **Supplementary Dataset 14**), as well as between *TNFSF4* expression in cycling *FOS*^{hi} T cells and mmDC proportions (**Fig. 6f** and **Supplementary Fig. 13e**; $\rho = 0.53$) (**Methods**,[68]). We also observed that AD prescription medications act on community 1 members by disrupting immune signaling through the IL-4/1L-13–IL-4Rα (dupilumab[69]), IL-31–IL-31Rα (nemolizumab[70]), and OX40L–OX40 (telazorlimab[71]) axes (**Supplementary Fig. 12j**).

Moreover, through extra-community interactions, community 1 likely impacts other components

of lesional AD skin, especially aberrant KC cornification. T effector cytokines *IL13*, *IL22* and *IL26* displayed putative interactions with KCs via *IL13RA1/IL4R*, *IL22RA1* and *IL20RA*, the latter highly expressed in cornified KCs and KC5, respectively (**Fig. 6e**). Moreover, *IL13* expression in cycling *FOS*^{hi} T cells was positively correlated to the proportions of KC5 and cornified KC1 cells (**Fig. 6f** and **Supplementary Fig. 13e**; $\rho = 0.57$ and 0.63), consistent with the known impact of type 2 cytokines on the expression of filaggrin and other cornified envelope components[72]. Together with the observed proportional shifts in those apical KC subsets and an altered KC trajectory in lesional skin (**Fig. 2j** and **Supplementary Fig. 7c**), this suggests an impact of KC-community 1 interactions on KC differentiation.

A cornified KC - *IL1B*$^{+}$ DC - neutrophil - T cell communication axis in AD

Within community 2, there were multiple putative interactions related to type 17 immunity and neutrophil recruitment (**Supplementary Fig. 13c**), two hallmarks of psoriasis[73]. *IL1B*$^{+}$ DCs had multiple putative interactions with neutrophils via *CXCL1/2/3/8-CXCR1/2* and with multiple T cell subsets including *IL13*$^{+}$/*IL22*$^{+}$/*IL26*$^{+}$ T cells and *CREM*^{hi} T and DCs (*e.g.*, mmDCs, *MMP12*$^{+}$ DC) via *CCL20-CCR6* (**Supplementary Fig. 13c**). These putative R-L interactions suggest possible cross-talk between community 2 and community 1 members, also reflected by partial overlap in the co-emergence of both communities (**Supplementary Fig. 12h** and **Supplementary Fig. 13d**), with *SPP1*$^{+}$ macrophages, *IL13*$^{+}$/*IL22*$^{+}$/*IL26*$^{+}$ T cells, and NK cells as shared components (**Supplementary Fig. 12h**). Both CXCL1/2/3/8-CXCR1/2 and CCL20-CCR6 have been implicated in mediating Th17 cell recruitment and polarization in psoriasis[73]. Consistently, *CCL20* expression in *IL1B*$^{+}$ DCs correlated positively with *CREM*^{hi} T cell proportions in lesional skin (**Supplementary Dataset 14;** $\rho = 0.56$).

Community 2 might be impacted by cornified KCs, which expressed high levels of *IL1* family cytokines and inhibitors and up-regulated the psoriasis disease genes *IL36G*, *IL36B* and *IL36RN*[74] (**Supplementary Fig. 13b**) in cornified KC1 in lesional skin (**Fig. 2k**). The IL36 receptor (*IL1RL2*) was mainly detected in KCs, LDCs and *IL1B*$^{+}$ DC, indicating intraepidermal signaling and cornified KC-DC crosstalk via IL36 (**Supplementary Fig. 13b**)[73]. Thus, a cornified KC-*IL1B*$^{+}$ DC-neutrophil-T cell communication axis may operate in inflammatory skin disease. Community 2 is detectable only in a subset of patients (**Supplementary Fig. 12b-d**), possibly reflecting proposed patient heterogeneity[61,75].

GWAS-nominated AD genes are enriched within the lesional multicellular community including *IL13*$^{+}$/*IL22*$^{+}$/*IL26*$^{+}$ T cells and in cornified keratinocytes

To relate our findings to AD genetic etiology, we examined genes associated with AD risk by GWAS to cell subsets in our skin cell atlas. We obtained disease-associated genes from a GWAS compendium of genome-wide significant genetic loci (2,678 studies, including 8 AD studies), using the OpenTargets Genetics Locus2Gene mapping[76], and from a recent genome-wide meta-analysis of AD (one-million individuals)[77,78]. We tested these genes for their enrichment in each of the 86 granular cell subset signatures, as well as in all lymphocyte gene programs (topics) (**Methods**).

Among cell subsets, AD GWAS gene expression was significantly enriched in *IL13*$^{+}$/*IL22*$^{+}$/*IL26*$^{+}$ T cells (Log OR: 3.37, FDR - $2.65*10^{-169}$, Fisher's exact test), cornified keratinocytes (Log OR: 2.91, FDR - 0.0148), DC2 CD83^{+}(Log OR: 3.21, FDR - 0.00301) and overall members of

multicellular community 1 (P value < 0.05, Fisher's exact test; **Supplementary Fig. 14a, red**; **Supplementary Dataset 14**). Consistently, among lymphocyte gene programs, topic #3-positive cells (with key TF regulators of Th2 fate *BHLHE40*[51] and *NFIL3*[79]) were the most enriched for AD GWAS genes (**Supplementary Fig. 14c**), as were topic #190 and #171 (with GWAS genes *IKZF3* and *TSHZ2*, implicated in T cell differentiation) (**Supplementary Fig. 14c,d**)[80]).

AD risk genes driving the cornified keratinocyte enrichment included *FLG*, located in the epidermal differentiation complex locus; *IL37*, an anti-inflammatory cytokine; and Gasdermin A (*GSDMA*), a member of a protein family involved in cell death and inflammation (**Supplementary Fig. 14e**). The *IL13*$^{+}$/*IL22*$^{+}$/*IL26*$^{+}$ T cell enrichment was driven by *IL13*, *CCR4*, *IL7R*, *IKZF1*, *RUNX3*, *CD274*, *CD6* and *THEMIS* (**Supplementary Fig. 14f**).

Finally, to highlight possible distinct and shared disease mechanisms, we expanded the scope of our enrichment analysis across GWAS of multiple skin and type 2 diseases (**Supplementary Fig. 14b; Supplementary Dataset 15**). Cornified KCs were associated with GWAS genes for AD, psoriasis and asthma, the latter ranking highest across tested diseases together with AD (**Supplementary Fig. 14b** and **Supplementary Fig. 14g**). AD, asthma, and allergic rhinitis were also among the top diseases displaying *IL13*$^{+}$/*IL22*$^{+}$/*IL26*$^{+}$ T cell-associated GWAS signal (**Supplementary Fig. 14h**), further supporting common genetic susceptibility and underlying mechanisms of these type 2 diseases[81].

Discussion

In this study, we mapped the cellular ecosystems of healthy and inflamed skin in AD by combining scRNA-seq with scTCR-seq. By establishing a rapid and efficient whole skin tissue processing

workflow without epidermal-dermal tissue layer separation, lengthy dissociation, or marker-based flow cytometry enrichment, we constructed a skin atlas that comprehensively captures the range of cells in skin tissue, especially rare or difficult-to-profile subsets, such as cornified keratinocytes. Through computational analysis of the atlas in the context of disease, we tie together pathologies at the genetic (risk genes), cellular and gene program, cell differentiation, and cell community levels, thus providing a tissue biology perspective to skin disease.

We found strong support for a unified multicellular model of disease, where lesional AD skin has an expanded immune compartment with the co-emergence of two multicellular immune/stromal communities – one present in all patients and another present only in a subset. These are connected to a pathological KC differentiation trajectory with increase in KC5 and early cornified cells (cKC1s) at the expense of terminally cornified cells (cKC2s), such that one community may help drive pathological KC differentiation and the other may be driven by it GWAS genes are particularly enriched in many of those components, closely tying the multicellular skin pathological state to the genetic drivers of the disease.

Disease-associated community 1 included clonally expanded $CD4^+$ and $CD8^+$ $IL13^+/IL22^+/IL26^+$ and cycling FOS^{hi} T cells with overlapping type 2, 22 and 17 characteristics, $MMP12^+$ DCs, $CCL17^{hi}CCL22^{hi}$ mregDC/mmDCs, $CCL19^+$ $IL4I1^+$ fibroblasts, and cycling ILCs, with multiple putative intercellular positive feedback loops that might contribute to its formation, stability and maintenance. Previous work reported the perivascular localization of $CCL19^+$ fibroblasts[8,82] and immune infiltrate enriched in DCs and T cells in the upper dermis[83,84], supporting the hypothesis that these community 1 cell types may be interacting in the AD dermis. At the core of community

1, cycling *FOS*^{hi} and *IL13*$^{+}$/*IL22*$^{+}$/*IL26*$^{+}$ T cells may be both recruited via *CCR4-CCL17/CCL22* and activated via *IL15* by mmDCs/mregDCs. *IL13*$^{+}$/*IL22*$^{+}$/*IL26*$^{+}$ T cells profiles resembled those of Th2A cells, a proallergic Th2 cell type previously reported across multiple allergic diseases[12,85], and of disease-associated T cells in eosinophilic esophagitis[86] and asthma[87], suggesting a common pathogenic state across type 2 diseases. Antigen-loaded mmDCs/mregDCs may further impact these T cells in a TCR-dependent manner and we hypothesize that antigen stimulation may contribute to the observed clonal expansion and increased cycling of *IL13*$^{+}$/*IL22*$^{+}$/*IL26*$^{+}$ T cells. Indeed, in the context of non-small cell lung cancer, antigen loading and presentation by mregDCs has been demonstrated and antigen uptake has been suggested to be a signal for mregDC generation[39]. Further studies are needed to test if ongoing antigen stimulation in lesional skin tissue is a contributor to the chronic inflammatory response; these could leverage TCR sequences from clonally-expanded, pathology-associated *IL13*$^{+}$/*IL22*$^{+}$/*IL26*$^{+}$ T cells, to characterize recognized antigens and elucidate mechanisms of antigen sensitization in the course of disease and therapy. Upon activation, *IL13*$^{+}$/*IL22*$^{+}$/*IL26*$^{+}$ T cells are in turn predicted to impact DCs, including mmDCs/mregDCs and *MMP12*$^{+}$ DCs through the myeloid cell activation and expansion factors *GM-CSF*, *FLT3LG*, *TNFSF4/OX40L* and *IL13* . This is consistent with the increase in STAT6 inferred activity in lesional *MMP12*$^{+}$ DCs and mmDCs/mregDCs, induction of IL13-STAT6 target genes (*e.g.*, *CCL17*, *IL4I1*), and shift in DC differentiation/activation trajectories to a partially activated *MMP12*$^{+}$ DC state in non-lesional skin and a fully activated mmDC/mregDC state in AD lesions. This fully activated mmDC/mregDCs state expresses both *CCL19* and its receptor *CCR7*, which may result in the attraction and clustering of mmDCs/mregDCs in DC-T rich areas[73,88].

Community 1 may play a key role in the pathological KC differentiation and cornification

trajectory we observed in AD lesional skin, which culminates in a less mature cornified KC1 subset, with lower expression of late cornified envelope constituents, and accumulation of non-fully differentiated KC5s (preceding cKC1s). This connection is supported by a significant correlation between the cell intrinsic expression of key cytokines *IL13* and *IL26* in T cells and the proportion of KC5s and cornified KC1s expressing their cognate receptors. This supports a model where IL13 directly affects terminal KC differentiation, consistent with reports of disrupted cornified gene expression in IL13-treated KCs *in vitro*[72]. Restoring the transition from cornified KC1s to cornified KC2s in AD might present an avenue for therapeutic barrier restoration.

In a subset of AD patients, we observed a second AD-associated community 2, with co-emergence of *IL1B*$^{+}$ DCs, *CREM*^{hi} T cells and neutrophils. *IL1B*$^{+}$ DCs described here displayed striking similarity to the recently described *IL23A*$^{+}$*IL1B*$^{+}$ DC3 subset, which was shown to be prevalent in psoriasis[38]. *IL1B*$^{+}$ DCs formed multiple putative interactions with neutrophils and expressed the Th17 regulators *CCL20* and *IL23A*. Varying amounts of skin-infiltrating neutrophils and type 17 expression signatures have been reported in previous AD patient cohorts, suggesting the presence of multiple AD endotypes[61,75]. Future studies in larger patient cohorts will further help stratify patient groups and will be able to corroborate patient heterogeneity in respect to community 2. One intriguing possibility is that community 2's formation may be impacted by aberrant KC differentiation, because cornified KCs, especially in lesional skin, express high levels of IL1 family cytokines and inhibitors, including up-regulation of the psoriasis disease genes *IL36G*, *IL36B* and *IL36RN*[74], and the IL36 receptor (*IL1RL2*) was expressed in detected in *IL1B*$^{+}$ DC.

The cell types and programs in the pathological circuit in lesional AD skin may be formed or

driven by genes associated with AD through GWAS. There is a significant enrichment of GWAS genes in cornified KCs, *IL13*$^{+}$/*IL22*$^{+}$/*IL26*$^{+}$ T cells, and multiple other community 1 and 2 cells, as well as in community 1 cells as a whole (but not community 2 as a whole). This agrees with a model of multiple routes to disease, where either epithelial or immune dysfunction and their interactions can initiate and then converge towards AD, and where genetic variants in multiple loci may affect the pathological formation of community 1 and its interaction with skin cornification through multiple feedback loops. Importantly, multiple key GWAS genes, such as *TNFSF4/OX40L* and *IL13* are part of the predicted intercellular feedback loops that could contribute to community 1 formation and maintenance and its interactions with KCs and their differentiation.

Together, our multi-modal fine-grained skin census provides insight into the remodeling of human skin under chronic inflammation, nominates targetable cellular states and transitions and serves as a fundamental resource towards a deeper understanding of skin biology.

Methods

Patient samples

Whole skin punch biopsy samples of 3-4mm diameter were obtained from sex matched atopic dermatitis patients (AD) patients, scleroderma patients, and healthy individuals after informed consent. Sample collection was conducted in accordance with protocols approved by Institutional Review Boards at Massachusetts General Hospital (protocol number 2018P002325) and Boston Children's Hospital (protocol number P00001109). and approval to the 2018P002325 and IRB-P00001109 studies at Massachusetts General Hospital and Boston Children's Hospital. Clinical information and metadata for the samples are provided in **SupplementaryData Fig. 1**. Healthy controls were individuals without a history of AD. Patients were included based on a clinical diagnosis of AD and were observed to have active disease via macroscopic assessment from a physician. Ethnicities were self-reported. A non-lesional and lesional biopsy were collected. Skin punch biopsies were immediately placed into tubes with cold DMEM containing 10% FBS, 2 mM L-glutamine and 100 U/ml penicillin/streptomycin (Thermo Scientific) and kept on ice until enzymatic dissociation.

Enzymatic dissociation of human whole skin punch biopsies

Whole skin punch biopsies (3-4mm) were cut into two pieces, such that each piece contains all skin layers and storage medium was removed. Enzymatic dissociation was performed using Whole Skin Dissociation kit (Miltenyi Biotec, #130-101-540) with a modified protocol. Cut biopsies were transferred into a gentleMACS C-tube containing 435µl Buffer L, 12.5µl Enzyme P, 50µl Enzyme D and 2.5µl Enzyme A. Enzymatic dissociation was performed for 3.5h at 37°C. After incubation, 500µl of cold DMEM containing 10% FBS and 2 mM L-glutamine were added. The tissue was

mechanically dissociated using a gentleMACS dissociator run on program h_skin_01. The resulting cellular suspension was filtered through a 70µm cell strainer (Falcon, #352350) and 4.5ml cold DMEM containing 10% FBS and 2 mM L-glutamine were added. Cells were spun down at 300g for 10min at 4°C. The supernatant was then aspirated and cells were resuspended in 1.2ml ACK buffer (A10492-01). Suspensions were transferred to 1.5ml tubes and incubated for 2min for red blood cell lysis and spun at 350g for 4min at 4°C. Supernatants were aspirated and cells were resuspended in 50-100µl 0.4% BSA in PBS. Cell viability and cell counts were determined and cells were processed for scRNA-seq.

Mouse model of AD-like inflammation using topical MC903 application

9 week old female C57BL/6J (strain #000664) mice were obtained from Jackson Laboratories (Bar Harbor, ME) and maintained in specific pathogen–free conditions in the animal facility of the Massachusetts General Hospital with a 12-h light:dark cycle, room temperature of 21 ^{o}C, and relative humidity of 30–70%. All experiments were approved by the Massachusetts General Hospital Subcommittee on Research Animal Care (Protocol number 2016N000203). A 2 cm x 2 cm patch of dorsal skin was carefully shaved 2 days before the initiation of treatment. 2 nM MC903 (R&D, Tocris, MN, USA) dissolved in ethanol or ethanol as control were topically applied daily for a period of 14 days. Mice were euthanized with CO_2 24 hours after the last treatment.

Enzymatic dissociation of mouse dorsal skin and flow cytometry

On the day of harvest, dorsal skin was shaved using hair clippers and the treated skin patch was harvested using scissors. Subcutaneous adipose tissue was removed, and skin tissue was transferred to cold PBS. Mouse skin was finely chopped using sterile razor blades, and the tissue was transferred into a gentleMACS C-tube containing 1.74ml Buffer L, 50µl Enzyme P, 200µl

Enzyme D and 10µl Enzyme A. Enzymatic dissociation was performed for 2.5h at 37°C and after incubation 2ml of DMEM containing 2% FBS and 10 mM HEPES at room temperature were added. Tissue was mechanically dissociated using a gentleMACS dissociator run on program h_skin_01 and for enzyme quenching 12µl 0.5M EDTA and 400µl FBS were added. The resulting cellular suspension was filtered through a 70µm cell strainer (Falcon, #352350) and cells were spun down at 400g for 10min at 4°C. Supernatant was aspirated and cells were resuspended in 1ml ACK buffer (A10492-01). Suspensions were transferred to 1.5ml tubes and incubated for 2min for red blood cell lysis and spun at 400g for 4min at 4°C. Supernatants were aspirated and cells were washed once in ice-cold fresh FACS buffer (PBS + 2% FCS + 2mM EDTA). Cells were resuspended in 500µl cold FACS buffer containing 1µl 7-AAD (Thermo Scientific) and filtered through a 40µm cap filter into FACS tubes. Viable cells (100.000 events) were sorted into 0.4% BSA in PBS on a Sony SH800 flow sorter. Cells were centrifuged at 400g for 10min at 4°C and supernatant was aspirated. Cells were resuspended in 0.4% BSA in PBS, counted and processed for scRNA-seq.

ScRNA-Seq and combined sc(5'-RNA and TCR)-seq

Cells were counted and ~8,000-12,000 cells were loaded per channel of the 10x Genomics Chromium chips using the 3'- v3 chemistry for scRNA-seq or the 5'- v1.1 chemistry for single-cell TCR- enriched V(D)J profiling. Single cells were processed through the 10x Genomics Chromium Platform according to manufacturer's instructions (10x Genomics). Briefly, cells were encapsulated into Gel Beads in Emulsion (GEMs) droplets using the Chromium instrument. For most AD samples, 2 10x channels were loaded given the availability of cells, whereas for most healthy and scleroderma samples, 1 channel was loaded. After encapsulation and cell lysis, cDNA

expression libraries were generated following the manufacturer's protocol, including barcoded reverse transcription, cDNA amplification, enzymatic fragmentation, adapter ligation and sample indexing steps. Libraries were quantified using Qubit dsDNA High Sensitivity assay kit (ThermoFisher Scientific). Fragment sizes of final libraries were assessed and quantified using DNA High Sensitivity Bioanalyzer Chip (Agilent), multiplexed and sequenced on either an Illumina Nextseq500, using a high output 150 cycle kit and the following read structure: Read 1: 28 cycles, Read 2: 96 cycles, Index Read 1: 8 cycles, or an Illumina NovaSeqS2 with the following read structure: Read 1: 28 cycles, Read 2: 90 cycles, Index Read 1: 10 cycles, Index Read 2: 10 cycles.

scRNA-seq data preprocessing

10X Cell Ranger v3 pipeline was used to align reads and generate count matrices, with the "cellranger mkfastq" and "cellranger count" commands, respectively. EmptyDrops function from the DropletUtils v1.6.1 R package was run on the unfiltered count matrices with ignore=10, retain=800 and lower=200 parameters with an FDR 1% cutoff. Barcodes with a total number of UMIs or genes < 200 were filtered out. Percent mitochondrial UMI cutoffs of 10% and 20% were used for the samples profiled with 10X v2 and v3 chemistry, respectively. Counts were normalized with a log(TP10K+1) transformation via the sc.pp.normalize_total function of Scanpy v1.8. Preprocessing and normalization steps were performed similarly for human scleroderma and mouse (control and MC903) scRNA-seq datasets. QC steps resulted in 29,689 and 9,133 high quality cell profiles in scleroderma and mouse datasets, respectively.

Annotation of coarse and granular cell subsets

PCA was performed with the top 2,000 highly variable genes and a *k*-nearest neighbor (*k*-NN)

graph was built with *k*=15 on 50 PCs using sc.pp.pca and sc.pp.neighbors functions of Scanpy, respectively. The *k*-NN graph was clustered with the Leiden community detection method[93,94] to partition cells into coarse clusters using the sc.tl.leiden in Scanpy. Marker genes were found using one-*vs*-rest two-tailed Welch's t-test using sc.tl.rank_genes_groups in Scanpy. For coarse cell type annotations, markers for each cluster were compared to literature-derived known markers. For the granular subset annotations, first, PCA was performed with the top 1,000 highly variable genes for each coarse cell type separately and a *k*-NN graph was built with *k*=15 on 50 PCs for each coarse cell type. Cells of the same coarse cell type were then clustered into more granular subsets using the Leiden algorithm with varying levels of resolution (ranging from 0.5 to 3.0) and were iteratively visualized with and without batch correction (PyTorch implementation of Harmony[95]). The harmonize() function from the PyTorch implementation of Harmony (https://github.com/lilab-bcb/harmony-pytorch[96]) was used with channel IDs as a batch covariate based on the PCA representation of cells for removing unwanted inter-sample and inter-individual variation. The cell subset markers, which were found similarly to the coarse cell type markers, were then compared with known literature markers in both batch-corrected and uncorrected views of the data. UMAP (Uniform Manifold Approximation and Projection)[97] was used for visualizations. Normalization, PCA, *k*-NN, data harmonization, clustering and data-driven marker identification steps were performed similarly to those of human healthy and AD samples. Only coarse cell types were annotated in mouse and scleroderma scRNA-seq datasets.

Differential expression

Negative binomial regression on raw counts using the diffxpy (https://github.com/theislab/diffxpy/releases, v0.1.7) Python package. '~ 1

+ sex + mt_frac +

log10_n_umis + disease_status' formula was used to compare healthy *vs*. lesional and healthy *vs*. non-lesional groups within each coarse and granular subset, while correcting for the fraction of mitochondrial UMIs, total number of UMIs and sex of the donor. Wald test was performed to estimate the effects of disease status.

Proportion analysis of single-cell and bulk RNA-seq data

The dirichreg function from the DirichletReg R package (v0.7) was used for testing the significance of differences in cell subset proportions across conditions for both scRNA-seq and deconvolved bulk RNA-seq. ‘'y ~ chemistry_10x + disease_status | disease_status” formula was used to fit the proportion models with the alternative parametrization for each cell subset separately in a one-*vs*-rest manner, with expected values and precision modeled by separate predictors. “chemistry_10x” refers to v2 or v3 chemistry (Chromium Single Cell 3’, 10x Genomics) and “disease_status” refers to whether the sample is healthy, non-lesional, or lesional. The effect of the “disease_status” variable was tested for significance using a likelihood ratio test, and FDR values were calculated from these p-values using the Benjamini-Hochberg method. FDR values are presented in the figures. The ggplot R package with the geom_boxplot2 function from the Ipaper R package was used for Box plot visualizations. geom_boxplot2 function was run with the “width.errorbar=0” argument. Lesional samples of patients BCH04 and BCH07 were excluded from the proportion analysis due to their lack of robust levels of epidermal inflammatory marker gene expression (**Supplementary Data Fig. 3f,g**).

Deconvolution of bulk RNA-seq

Bulk RNA-seq data[19] were downloaded from Gene Expression Omnibus (GEO, accession GSE121212). Psoriasis samples were discarded. The ag.optimize function from the autogenes Python package[98] was run on log(TPM+1)-transformed scRNA-seq expression values with the arguments "ngen=5000, seed=0, nfeatures=400, mode='fixed', offspring_size=100". Granular subset annotations were used for the marker optimization. Next, the ad.deconvole function was run with the NuSVR method on log(TPM+1) transformed bulk RNA-seq expression values. Negative weights were set to zero.

Preprocessing of published skin scRNA-seq data

Raw counts of published scRNA-seq were downloaded either from GEO (GSE158432[12], GSE153760[11], GSE147424[8]) or the HCA skin portal[10] at https://developmentcellatlas.ncl.ac.uk/datasets/hca_skin_portal/.

Cell type classification

A multinomial logistic ridge regression classifier was used to classify cell profiles from the published scRNA-seq skin datasets, and the 5' scRNA-seq and scleroderma scRNA-seq datasets in this study. log(TP10k+1)-transformed expression values were concatenated across the published scRNA-seq skin datasets and the present study for a total of 921,832 cells. To maintain comparable regression coefficients across genes, z-score-transformed expression values across the five datasets were used for the fit. Protein coding genes were filtered for expression in at least 30 cells for the classification, which resulted in 17,494 genes.

LogisticRegressionCV class from scikit-learn Python package was instantiated with parameters

"class_weight='balanced', scoring='balanced_accuracy', n_jobs=12, Cs=numpy.logspace(-6, -4, 20))" to determine the *L*2 regularization coefficient via stratified 5-fold cross-validation with a balanced accuracy metric.

To classify the (5'RNA + TCR)-seq dataset, mean expression was subtracted and multiplied with standard deviation values calculated across the cells in five datasets to bring the expression levels to the same level as the rest.

Graph abstraction analysis

For the undirected and directed PAGA graphs, sc.tl.paga and scv.tl.paga functions were used from Scanpy and scVelo packages, respectively. In the directed PAGA analysis of DC subsets (**Fig. 3c)**, RNA velocity values (below) were used with velocity pseudotime as a prior to determine the directionality.

RNA velocity

Velocyto.py command line interface (v0.17.15)[24] was used to count spliced and unspliced reads using the "velocyto run possorted_genome_bam.bam cellranger-GRCh38-3.0.0-genes.gtf -o sample -m hg38_rmsk.gtf -b barcodes_sample.csv -@ 30 -vv --samtools-memory 100000 -e sample" command. Repetitive elements were masked using the RepeatMasker track downloaded from UCSC Genome Browser in GTF format. Downstream analysis was performed using the scv.pp.moments, scv.tl.recover_dynamics, scv.tl.velocity, scv.tl.paga, and scv.tl.velocity_pseudotime functions of scVelo (v0.2.1)[25]. scv.tl.velocity was run in stochastic and dynamical modes for DCs and KCs, respectively. Patients BCH01, BCH04, BCH07 were excluded in the RNA velocity analysis of keratinocytes due to high inter-individual variation introduced by

these samples.

Pseudotime trajectories of keratinocytes and dendritic cells

For the keratinocyte pseudotime trajectories, KC 5, cKC1 and cKC2 subsets were first subsetted from all keratinocytes (healthy, non-lesional, lesional). PCA was calculated using the top 500 highly variable genes. Inter-individual effects were removed using the harmonize() function in the PyTorch version of Harmony[96] based on PCA representation of cells (50 PCs) with individual IDs as batch covariate. *k*-NN graph was built using batch corrected Harmony representations with 150 neighbors (*k*=150). sc.tl.diffmap and sc.tl.dpt in Scanpy[26,99] to calculate the trajectories. cKC populations were collapsed to gain more statistical power.

For the dendritic cell pseudotime trajectories, we used the latent time inference based on the RNA velocities of six DC subsets (mmDC, *MMP12*$^+$ DC, Langerhans cells, DC2s, *CD83*$^+$ DCs, *IL1B*$^+$ DCs), as inferred by scVelo (described above). scv.tl.latent_time function was used to unify the gene-specific latent timepoints into a universal latent time.

Pseudotime distributions were plotted using the Python implementation of grammar of graphics, plotnine (https://github.com/has2k1/plotnine, version 0.8). Comparison of pseudotime distributions between conditions were performed using the scipy.stats.mannwhitneyu function.

Gene set enrichment analysis

The sc.queries.enrich function from Scanpy was used for gene set enrichment analysis with REACTOME gene sets and the arguments “gprofiler_kwargs={'no_evidences': False,

'sources':['REAC'], 'all_results': True}". FDR < 0.1 and log_2(fold change) > 0.5 cutoffs were used for fibroblast and KC marker analyses. For differentially expressed genes between healthy vs lesional KCs, FDR < 0.1 and log2 fold change > 1 cutoffs were used.

Topic modeling of lymphocytes

A stochastic block model-based hierarchical topic modeling approach[49] (https://github.com/martingerlach/hSBM_Topicmodel) was used. The number of topics (253) was determined automatically during the SBM inference using the minimum description length-based Bayesian model selection approach. For visualization of differential topic weights between conditions, an empirical cumulative distribution function (ECDF) of topic weights was calculated by the distributions.empirical_distribution ECDF function from the statsmodels Python package (v0.11.1).

T cells with topic 190 (pathological T cell topic) weights greater than the 90th percentile of the weight distribution of this topic (0.0049) were assigned the label of "T *IL13*$^+$*/IL22*$^+$*/IL26*$^+$".

Differential expression of lymphocyte topics between conditions

Differential expression analysis of topic expression was performed using Welch's two-sided *t* test (sc.tl.rank_genes_groups function in Scanpy). Benjamini-Hochberg FDR values are used in the figures. ggplot function from the plotnine plotting package was used for visualizations of the DE results.

Correlation analysis of cytokine programs

The corrcoef function in the NumPy Python package was used to find genes correlated with *IL5, IL13, IL22, IL26, IL31* within lymphocytes. Barplot visualizations were produced using the plotnine (v0.7) Python package.

TF activity analysis

The Python implementation of Dorothea (https://github.com/saezlab/dorothea-py, commit=5e3ee0e)[100,101] was used to calculate the activity scores of 118 transcription factors, which are in A and B confidence categories of Dorothea, for each cell. dorothea.run function was used with "dorothea.load_regulons(['A', 'B']), center=True, scale=True, use_raw=False" arguments.

For the healthy vs. lesional and non-lesional differential activity analysis, a linear regression model for each cell subset was fit with the formula "score ~ 1 + sex + mt_frac + log10_n_umis + disease_status" where disease_status is a binary variable indicating whether a cell has healthy or lesional/non-lesional status. statsmodels.formula.api.ols function from the statsmodels Python package (v0.11.1) was used for the regression analysis.

Preprocessing and analysis of joint single cell (5'RNA + TCR)-seq

Fastq, h5 and JSON files representing the reads, 5' gene expression and VDJ information were o obtained with Cell Ranger (v2.0.2) V(D)J pipeline commands "cellranger mkfastq" and "cellranger vdj".

Scirpy[102] (v0.5.0) was used for the TCR analysis. First, for each patient, TCR data were loaded in json format using the ir.io.read_10x_vdj function with "patient_tcr.json', filtered=True"

arguments. After merging 5' scRNA-seq expression data with TCR information, PCA was fitted with top 2,000 highly variable genes on the log(TP10K+1)-normalized expression matrix. Graph-based Leiden clustering was run with resolution=1.0 parameter on the *k*-NN graph built with *k*=15 on 50 PCs to annotate the T cell cluster which showed high *CD3D* and *CD3E* expression. Only cells in this cluster that also have TCR information were retained for downstream analysis, yielding 1,138 cells from two patients. Granular cell subset annotations were predicted using both the cell subset classifier trained on the 3' scRNA-seq data and a pretrained SCimilarity foundation model[103] (https://zenodo.org/records/10685499). These annotations were used to subset the 7,256 total T cells to 6,047 $CD4^+$ T cells, which were used in the subsequent topic 190 analysis.

Data from each patient were merged and integrated using the harmonize() function of the PyTorch implementation of Harmony[96] similarly to the procedure described in the "Annotation of coarse and granular cell subsets" subsection. Clonotypes were determined jointly using the amino acid sequences of the CDR3 region on the VDJ receptor arms (TCR-β, TCR-δ, and IG-heavy chains) by the ir.pp.ir_neighbors(adata, sequence='aa', receptor_arms='VDJ') and ir.tl.define_clonotype_clusters(adata) functions of Scirpy, where a clone is defined as all cells with an identical VDJ CDR3 amino acid sequence. Clones of two or more were labeled as expanded.

Two-tailed Welch's t-test via sc.tl.rank_genes_groups function from the Scanpy Python package was used to identify genes differentially expressed between cells from expanded (n>=2) *vs*. non-expanded (n=1) clones. sc.tl.score_genes function in Scanpy was used with genes that have non-zero probabilities in Topic 190 (**Supplementary Dataset 10**) to calculate the average expression of Topic 190 in the T cells with VDJ information. scipy.stats.zscore function was used to z-score

the calculated Topic 190 scores.

Sample PCA by granular cell subset proportions

Granular cell type proportions (including the *IL13*$^+$/*IL22*$^+$/*IL26*$^+$ T cell subset) of each channel were 'centered log-ratio' (CLR)-transformed using the 'clr' function from the 'composition_stats' Python package. For PCA embeddings of channels, the sc.pp.pca() function from Scanpy package was used with the CLR-transformed proportions. BCH01 non-lesional channels (BCH01-NL1 and BCH01-NL2) were not used in the analysis since these samples have absolute z-score proportion values beyond 2.0 in 29 (BCH01-NL1) and 32 (BCH01-NL2) out of 87 cell subsets. Proportions shown in the heatmaps and PCA scatterplots (**Fig. 6a** and **Supplementary Data Figure 12a,d,g**) are z- score-transformed.

Granular cell type embeddings using proportions

Granular cell subset proportions (including *IL13*$^+$/*IL22*$^+$/*IL26*$^+$ T cells) were calculated for each channel. After CLR and z-score transformations, cell subsets in the transposed matrix (cell subset × channel) were embedded by UMAP with a *k*-NN graph representation (*k*=20) of cell subsets. sc.pp.neighbors and sc.tl.umap functions were used for the embedding. clr() function from the composition-stats Python package (v2.0.0) was used for the centered log-ratio transform. BCH01 non-lesional channels (BCH01-NL1 and BCH01-NL2) were excluded from the analysis as explained above.

Correlation of cell subsets

Spearman correlation coefficients of the granular cell subset proportion profiles for each pair of

samples were calculated using the DataFrame.corr() function of Pandas Python package with the method='spearman' argument. Correlations were visualized as a heat map using the 'clustermap' function from the Seaborn Python package.

Receptor-ligand analysis

Putative cell-cell interactions were identified between cell subsets that are significant in at least one lesional channel using the command line interface of CellPhoneDB v2.1[104] ("cellphonedb method statistical_analysis meta.tsv counts.tsv --counts-data hgnc_symbol --project-name ad --threads 90 --subsampling --subsampling-num-cells 3000 --subsampling-log false"). This method identifies specific cell-cell interactions by performing empirical shuffling across cell-type pairs and calculating the ligand–receptor pairs displaying significant cell-type specificity. Next, z-score-transformed expression levels of the receptor and ligand were calculated. For a cell subset of interest, z-score within the coarse cell type was used, whereas for the other cell subsets potentially interacting with the cell subset of interest, a global z-score across cell types was used. Finally, significant receptor or ligand genes that are highly expressed in either cell subset of interest or its partners were manually selected using the mean z-score of the receptor and ligand expression. For the *IL13*$^+$/*IL22*$^+$/*IL26*$^+$ T cell subset, gene selections were made based on expression cutoffs (z-score > 1.0) instead of the CellPhoneDB significance.

For receptor cell frequency and ligand mean expression correlations[68], granular cell subset proportions across lesional sample channels that had at least six cells expressing the ligand gene (log(TP10K+1) > 0) were used. Z-score-transformed sample-level mean expression values were correlated with cell type proportions using the DataFrame.corr() function from the Pandas Python

package (version 1.3.5) with “spearman” parameter.

Non-human primate data preprocessing and integration

A *Macaca mulatta* DRG sensory neuron scRNA-seq dataset[52] was downloaded from GEO (GSE165566). The top 2,000 highly variable genes were identified using the sc.pp.highly_variable_genes function of Scanpy. PCA was fitted using the highly variable genes. Next, data across three profiled individuals was integrated using the PyTorch implementation of Harmony in the PC space with 50 PCs and a *k*-nearest neighbors (*k*-NN) graph (*k*=15) was constructed using batch-corrected Harmony representation of cells using harmony.harmonize(adata.obsm['X_pca'], adata.obs, 'sample_name') and sc.pp.neighbors(adata, use_rep='X_harmony') functions. The cell type annotations provided by the authors were used.

GWAS enrichment analysis

GWAS-nominated genes for 2,963 diseases and traits were downloaded from the Open Targets Genetics (OTG)[76] GraphQL API (https://github.com/opentargets/genetics-api, v20.02). Additional AD GWAS-nominated genes were obtained from a genome-wide meta-analysis of one-million individuals[77,78] (obtained from Table 1 and Supplementary Table S1 in ref[78]). Fisher’s exact test, implemented in Fisher python package, was used to test gene sets nominated by the Locus2Gene (L2G) framework of OTG for a particular phenotype were enriched in markers of each of the 86 cell subsets and of the *IL13*$^{+}$/*IL22*$^{+}$/*IL26*$^{+}$ T cell subset, for a total of 87 cell subsets tested. Cell subset marker genes were defined in six different ways and each tested for enrichment. First, three types of markers were defined as (**1**) genes with higher than z-score of 1.0; (**2**) genes with top 200 highest z-score values; (**3**) genes with top 50 highest z-score values. In each of these three cases,

z-scores were calculated either (**1**) across all cells (*i.e.*, global marker signatures); or (**2**) across cells within each coarse cell type annotation (*i.e.*, local marker signatures), overall yielding six gene sets for each of the 86 granular subsets. GWAS enrichment analyses were performed with 87 subsets.

For the AD GWAS gene set, the union of genes nominated in GWAS were used, where the trait name is one of eczema, atopic dermatitis, "inflammatory skin disease [Atopic dermatitis", "atopic dermatitis [random effects]", "atopic dermatitis [EA, fixed effects]", "Eczema/dermatitis | non-cancer illness code, self-reported" in the OTG trait list. This led to 9 GWAS, including 8 published studies[6,105–111], and the UK Biobank GWAS round 2 results of Neale lab (http://www.nealelab.is/uk-biobank).

Data availability

Data associated with this work is available at the Gene Expression Omnibus (GEO) under accession GSE204765 [https://www.ncbi.nlm.nih.gov/geo/query/acc.cgi?acc=GSE204765]. Raw fastq files for adult samples are deposited on dbGAP as controlled access data under accession phs004337.v1.p1 (https://www.ncbi.nlm.nih.gov/projects/gap/cgi-bin/study.cgi?study_id=phs004337.v1.p1). Raw fastq files for pediatric samples cannot be deposited in a public repository because of restrictions in the informed consent, and may be requested from L.S. (Lynda.Schneider@childrens.harvard.edu). Dr. Schneider will respond to requests within two weeks; access to data will be granted after individuals are added to the IRB, appropriate institutional approvals will typically be completed within two months. Processed scRNA-seq data of the current study and the curated Atopic Dermatitis Atlas are available at https://cellxgene.cziscience.com/collections/5e143645-177c-45b6-952d-48770e29a54b,

https://singlecell.broadinstitute.org/single_cell/study/SCP2613, and https://singlecell.broadinstitute.org/single_cell/study/SCP2738. The scleroderma data and the mmDCs from our AD study and public studies are available at https://singlecell.broadinstitute.org/single_cell/study/SCP3122 and https://singlecell.broadinstitute.org/single_cell/study/SCP3120 respectively. The 5'-scRNA-Seq + scTCR-Seq dataset is available at https://singlecell.broadinstitute.org/single_cell/study/SCP3036. Source data are provided with this paper.

Code availability

Code for all analyses is available on GitHub: https://doi.org/10.5281/zenodo.17211367

References

1. Langan, S. M., Irvine, A. D. & Weidinger, S. Atopic dermatitis. *Lancet* **396**, 345–360 (2020).

2. Jungersted, J. M. *et al.* Stratum corneum lipids, skin barrier function and filaggrin mutations in patients with atopic eczema. *Allergy* **65**, 911–918 (2010).

3. Sanyal, R. D. *et al.* Atopic dermatitis in African American patients is T2/T22-skewed with T1/T17 attenuation. *Ann. Allergy Asthma Immunol.* **122**, 99–110.e6 (2019).

4. Nettis, E. *et al.* Use of Dupilumab in 543 Adult Patients With Moderate-to-Severe Atopic Dermatitis: A Multicenter, Retrospective Study. *J. Investig. Allergol. Clin. Immunol.* **32**, 124–132 (2022).

5. Renert-Yuval, Y. & Guttman-Yassky, E. New treatments for atopic dermatitis targeting beyond IL-4/IL-13 cytokines. *Ann. Allergy Asthma Immunol.* **124**, 28–35 (2020).

6. Paternoster, L. *et al.* Meta-analysis of genome-wide association studies identifies three new risk loci for atopic dermatitis. *Nat. Genet.* **44**, 187–192 (2011).

7. Stubbington, M. J. T., Rozenblatt-Rosen, O., Regev, A. & Teichmann, S. A. Single-cell transcriptomics to explore the immune system in health and disease. *Science* **358**, 58–63 (2017).

8. He, H. *et al.* Single-cell transcriptome analysis of human skin identifies novel fibroblast subpopulation and enrichment of immune subsets in atopic dermatitis. *J. Allergy Clin. Immunol.* **145**, 1615–1628 (2020).

9. Hughes, T. K. *et al.* Second-Strand Synthesis-Based Massively Parallel scRNA-Seq Reveals Cellular States and Molecular Features of Human Inflammatory Skin Pathologies. *Immunity* **53**, 878–894.e7 (2020).

10. Reynolds, G. *et al.* Developmental cell programs are co-opted in inflammatory skin disease. *Science* **371**, (2021).

11. Rojahn, T. B. *et al.* Single-cell transcriptomics combined with interstitial fluid proteomics defines cell type-specific immune regulation in atopic dermatitis. *J. Allergy Clin. Immunol.* **146**, 1056–1069 (2020).

12. Bangert, C. *et al.* Persistence of mature dendritic cells, TH2A, and Tc2 cells characterize clinically resolved atopic dermatitis under IL-4Rα blockade. *Science immunology* **6**, (2021).

13. Cheng, J. B. *et al.* Transcriptional Programming of Normal and Inflamed Human Epidermis at Single-Cell Resolution. *Cell Rep.* **25**, 871–883 (2018).

14. Wang, S. *et al.* Single cell transcriptomics of human epidermis identifies basal stem cell transition states. *Nat. Commun.* **11**, 4239 (2020).

15. Gur, C. *et al.* LGR5 expressing skin fibroblasts define a major cellular hub perturbed in scleroderma. *Cell* **185**, 1373–1388.e20 (2022).

16. Jin, S.-P. *et al.* Mapping the immune cell landscape of severe atopic dermatitis by single-cell RNA-seq. *Allergy* **79**, 1584–1597 (2024).

17. Tamminga, S. M. *et al.* Single-cell sequencing of human Langerhans cells identifies altered gene expression profiles in patients with atopic dermatitis. *ImmunoHorizons* **9**, (2025).

18. Zhang, B. *et al.* Single-cell profiles reveal distinctive immune response in atopic dermatitis in contrast to psoriasis. *Allergy* **78**, 439–453 (2023).

19. Tsoi, L. C. *et al.* Atopic Dermatitis Is an IL-13-Dominant Disease with Greater Molecular Heterogeneity Compared to Psoriasis. *J. Invest. Dermatol.* **139**, 1480–1489 (2019).

20. Candi, E., Schmidt, R. & Melino, G. The cornified envelope: a model of cell death in the skin. *Nat. Rev. Mol. Cell Biol.* **6**, 328–340 (2005).

21. Fuchs, E. & Raghavan, S. Getting under the skin of epidermal morphogenesis. *Nat. Rev. Genet.* **3**, 199–209 (2002).

22. Wolf, F. A. *et al.* PAGA: graph abstraction reconciles clustering with trajectory inference through a topology preserving map of single cells. *Genome Biol.* **20**, 59 (2019).

23. Akinduro, O. *et al.* Constitutive Autophagy and Nucleophagy during Epidermal Differentiation. *J. Invest. Dermatol.* **136**, 1460–1470 (2016).

24. La Manno, G. *et al.* RNA velocity of single cells. *Nature* **560**, 494–498 (2018).

25. Bergen, V., Lange, M., Peidli, S., Wolf, F. A. & Theis, F. J. Generalizing RNA velocity to transient cell states through dynamical modeling. *Nat. Biotechnol.* **38**, 1408–1414 (2020).

26. Haghverdi, L., Büttner, M., Wolf, F. A., Buettner, F. & Theis, F. J. Diffusion pseudotime robustly reconstructs lineage branching. *Nat. Methods* **13**, 845–848 (2016).

27. de Guzman Strong, C. *et al.* Lipid defect underlies selective skin barrier impairment of an epidermal-specific deletion of Gata-3. *J. Cell Biol.* **175**, 661–670 (2006).

28. Ting, S. B. *et al.* A homolog of Drosophila grainy head is essential for epidermal integrity in mice. *Science* **308**, 411–413 (2005).

29. Mills, A. A. *et al.* p63 is a p53 homologue required for limb and epidermal morphogenesis. *Nature* **398**, 708–713 (1999).

30. Mitamura, Y. *et al.* The IL-13/periostin/IL-24 pathway causes epidermal barrier dysfunction in allergic skin inflammation. *Allergy* **73**, 1881–1891 (2018).

31. Lachner, J., Mlitz, V., Tschachler, E. & Eckhart, L. Epidermal cornification is preceded by the expression of a keratinocyte-specific set of pyroptosis-related genes. *Sci. Rep.* **7**, 17446 (2017).

32. Li, M. *et al.* Topical vitamin D3 and low-calcemic analogs induce thymic stromal lymphopoietin in mouse keratinocytes and trigger an atopic dermatitis. *Proc. Natl. Acad. Sci. U. S. A.* **103**, 11736–11741 (2006).

33. Joost, S. *et al.* Single-Cell Transcriptomics Reveals that Differentiation and Spatial Signatures Shape Epidermal and Hair Follicle Heterogeneity. *Cell Syst* **3**, 221–237.e9 (2016).

34. Kim, B. S. *et al.* Basophils promote innate lymphoid cell responses in inflamed skin. *J. Immunol.* **193**, 3717–3725 (2014).

35. Leyva-Castillo, J. M. *et al.* Single-cell transcriptome profile of mouse skin undergoing antigen-driven allergic inflammation recapitulates findings in atopic dermatitis skin lesions. *J. Allergy Clin. Immunol.* **150**, 373–384 (2022).

36. Jaitin, D. A. *et al.* Lipid-Associated Macrophages Control Metabolic Homeostasis in a Trem2-Dependent Manner. *Cell* **178**, 686–698.e14 (2019).

37. Villani, A.-C. *et al.* Single-cell RNA-seq reveals new types of human blood dendritic cells, monocytes, and progenitors. *Science* **356**, (2017).

38. Nakamizo, S. *et al.* Single-cell analysis of human skin identifies CD14+ type 3 dendritic cells co-producing IL1B and IL23A in psoriasis. *J. Exp. Med.* **218**, (2021).

39. Maier, B. *et al.* A conserved dendritic-cell regulatory program limits antitumour immunity. *Nature* **580**, 257–262 (2020).

40. Hamilton, J. D. *et al.* Dupilumab improves the molecular signature in skin of patients with moderate-to-severe atopic dermatitis. *J. Allergy Clin. Immunol.* **134**, 1293–1300 (2014).

41. Zhang, Q. *et al.* Landscape and Dynamics of Single Immune Cells in Hepatocellular Carcinoma. *Cell* **179**, 829–845.e20 (2019).

42. Zilionis, R. *et al.* Single-Cell Transcriptomics of Human and Mouse Lung Cancers Reveals Conserved Myeloid Populations across Individuals and Species. *Immunity* **50**, 1317–1334.e10 (2019).

43. Gao, Y. *et al.* Control of T helper 2 responses by transcription factor IRF4-dependent

dendritic cells. *Immunity* **39**, 722–732 (2013).

44. Tubo, N. J., McLachlan, J. B. & Campbell, J. J. Chemokine receptor requirements for epidermal T-cell trafficking. *Am. J. Pathol.* **178**, 2496–2503 (2011).

45. Kumamoto, Y. *et al.* CD301b^{+} dermal dendritic cells drive T helper 2 cell-mediated immunity. *Immunity* **39**, 733–743 (2013).

46. Dixit, A. *et al.* Perturb-Seq: Dissecting Molecular Circuits with Scalable Single-Cell RNA Profiling of Pooled Genetic Screens. *Cell* **167**, 1853–1866.e17 (2016).

47. Martin, J. C. *et al.* Single-Cell Analysis of Crohn's Disease Lesions Identifies a Pathogenic Cellular Module Associated with Resistance to Anti-TNF Therapy. *Cell* **178**, 1493–1508.e20 (2019).

48. Bielecki, P. *et al.* Skin-resident innate lymphoid cells converge on a pathogenic effector state. *Nature* **592**, 128–132 (2021).

49. Gerlach, M., Peixoto, T. P. & Altmann, E. G. A network approach to topic models. *Sci Adv* **4**, eaaq1360 (2018).

50. Bapat, S. P. *et al.* Obesity alters pathology and treatment response in inflammatory disease. *Nature* **604**, 337–342 (2022).

51. Henriksson, J. *et al.* Genome-wide CRISPR Screens in T Helper Cells Reveal Pervasive Crosstalk between Activation and Differentiation. *Cell* **176**, (2019).

52. Kupari, J. *et al.* Single cell transcriptomics of primate sensory neurons identifies cell types associated with chronic pain. *Nat. Commun.* **12**, 1510 (2021).

53. Antúnez, C. *et al.* Different cytokine production and activation marker profiles in circulating cutaneous-lymphocyte-associated antigen T cells from patients with acute or chronic atopic dermatitis. *Clin. Exp. Allergy* **34**, 559–566 (2004).

54. Halim, T. Y. F. *et al.* Tissue-Restricted Adaptive Type 2 Immunity Is Orchestrated by Expression of the Costimulatory Molecule OX40L on Group 2 Innate Lymphoid Cells. *Immunity* **48**, 1195–1207.e6 (2018).

55. Yomogida, K. *et al.* Hobit confers tissue-dependent programs to type 1 innate lymphoid cells. *Proc. Natl. Acad. Sci. U. S. A.* **118**, (2021).

56. Mackay, L. K. *et al.* Hobit and Blimp1 instruct a universal transcriptional program of tissue residency in lymphocytes. *Science* **352**, 459–463 (2016).

57. Buechler, M. B. *et al.* Cross-tissue organization of the fibroblast lineage. *Nature* **593**, 575–579 (2021).

58. Kinchen, J. *et al.* Structural Remodeling of the Human Colonic Mesenchyme in Inflammatory Bowel Disease. *Cell* **175**, 372–386.e17 (2018).

59. Madissoon, E. *et al.* A spatially resolved atlas of the human lung characterizes a gland-associated immune niche. *Nat. Genet.* **55**, 66–77 (2022).

60. Nayar, S. *et al.* Immunofibroblasts are pivotal drivers of tertiary lymphoid structure formation and local pathology. *Proc. Natl. Acad. Sci. U. S. A.* **116**, 13490–13497 (2019).

61. Dhingra, N. *et al.* Attenuated neutrophil axis in atopic dermatitis compared to psoriasis reflects TH17 pathway differences between these diseases. *J. Allergy Clin. Immunol.* **132**, 498–501.e3 (2013).

62. Wang, A. *et al.* Cytokine RNA in situ hybridization permits individualized molecular phenotyping in biopsies of psoriasis and atopic dermatitis. *JID Innov.* **1**, 100021 (2021).

63. Schäbitz, A. *et al.* Spatial transcriptomics landscape of lesions from non-communicable inflammatory skin diseases. *Nat. Commun.* **13**, 7729 (2022).

64. Waldmann, T. A. The biology of interleukin-2 and interleukin-15: implications for cancer

therapy and vaccine design. *Nat. Rev. Immunol.* **6**, 595–601 (2006).

65. Anderson, D. M. *et al.* A homologue of the TNF receptor and its ligand enhance T-cell growth and dendritic-cell function. *Nature* **390**, 175–179 (1997).

66. Ingelfinger, F., De Feo, D. & Becher, B. GM-CSF: Master regulator of the T cell-phagocyte interface during inflammation. *Semin. Immunol.* **54**, 101518 (2021).

67. Waskow, C. *et al.* The receptor tyrosine kinase Flt3 is required for dendritic cell development in peripheral lymphoid tissues. *Nat. Immunol.* **9**, 676–683 (2008).

68. Smillie, C. S. *et al.* Intra- and Inter-cellular Rewiring of the Human Colon during Ulcerative Colitis. *Cell* vol. 178 714–730.e22 Preprint at https://doi.org/10.1016/j.cell.2019.06.029 (2019).

69. Drugs for Atopic Dermatitis. *Med. Lett. Drugs Ther.* **62**, 89–96 (2025).

70. Nemolizumab (Nemluvio) for atopic dermatitis. *Med. Lett. Drugs Ther.* **67**, 25–27 (2025).

71. Rewerska, B. *et al.* Phase 2b randomized trial of OX40 inhibitor telazorlimab for moderate-to-severe atopic dermatitis. *J. Allergy Clin. Immunol. Glob.* **3**, 100195 (2024).

72. Howell, M. D. *et al.* Cytokine modulation of atopic dermatitis filaggrin skin expression. *J. Allergy Clin. Immunol.* **124**, R7–R12 (2009).

73. Kim, T.-G. *et al.* Dermal clusters of mature dendritic cells and T cells are associated with the CCL20/CCR6 chemokine system in chronic psoriasis. *J. Invest. Dermatol.* **134**, 1462–1465 (2014).

74. Marrakchi, S. *et al.* Interleukin-36-receptor antagonist deficiency and generalized pustular psoriasis. *N. Engl. J. Med.* **365**, 620–628 (2011).

75. Guttman-Yassky, E. & Krueger, J. G. Atopic dermatitis and psoriasis: two different

immune diseases or one spectrum? *Curr. Opin. Immunol.* **48**, 68–73 (2017).

76. Mountjoy, E. *et al.* An open approach to systematically prioritize causal variants and genes at all published human GWAS trait-associated loci. *Nat. Genet.* **53**, 1527–1533 (2021).

77. Budu-Aggrey, A. *et al.* European and multi-ancestry genome-wide association meta-analysis of atopic dermatitis highlights importance of systemic immune regulation. *Nat. Commun.* **14**, 6172 (2023).

78. Pasanen, A. *et al.* Identifying atopic dermatitis risk loci in 1,094,060 individuals with subanalysis of disease severity and onset. *J. Invest. Dermatol.* **144**, 2417–2425 (2024).

79. Kashiwada, M., Cassel, S. L., Colgan, J. D. & Rothman, P. B. NFIL3/E4BP4 controls type 2 T helper cell cytokine expression. *EMBO J.* **30**, 2071–2082 (2011).

80. Powell, M. D., Read, K. A., Sreekumar, B. K. & Oestreich, K. J. Ikaros Zinc Finger Transcription Factors: Regulators of Cytokine Signaling Pathways and CD4 T Helper Cell Differentiation. *Front. Immunol.* **10**, 1299 (2019).

81. Ferreira, M. A. *et al.* Shared genetic origin of asthma, hay fever and eczema elucidates allergic disease biology. *Nat. Genet.* **49**, 1752–1757 (2017).

82. Shi, Z. *et al.* The role of dermal fibroblasts in autoimmune skin diseases. *Front. Immunol.* **15**, 1379490 (2024).

83. Pan, Y. *et al.* The roles of innate immune cells in atopic dermatitis. *J. Innate Immun.* **16**, 385–396 (2024).

84. Bowcock, A. M. & Krueger, J. G. Getting under the skin: the immunogenetics of psoriasis. *Nat. Rev. Immunol.* **5**, 699–711 (2005).

85. Rindler, K. *et al.* Spontaneously resolved atopic dermatitis shows melanocyte and immune cell activation distinct from healthy control skin. *Front. Immunol.* **12**, 630892 (2021).

86. Morgan, D. M. *et al.* Clonally expanded, GPR15-expressing pathogenic effector TH2 cells are associated with eosinophilic esophagitis. *Science immunology* **6**, (2021).

87. Vieira Braga, F. A. *et al.* A cellular census of human lungs identifies novel cell states in health and in asthma. *Nat. Med.* **25**, 1153–1163 (2019).

88. Natsuaki, Y. *et al.* Perivascular leukocyte clusters are essential for efficient activation of effector T cells in the skin. *Nat. Immunol.* **15**, 1064–1069 (2014).

89. Uhlén, M. *et al.* Proteomics. Tissue-based map of the human proteome. *Science* **347**, 1260419 (2015).

90. Jassal, B. *et al.* The reactome pathway knowledgebase. *Nucleic Acids Res.* **48**, D498–D503 (2020).

91. Solé-Boldo, L. *et al.* Single-cell transcriptomes of the human skin reveal age-related loss of fibroblast priming. *Commun Biol* **3**, 188 (2020).

92. Philippeos, C. *et al.* Spatial and Single-Cell Transcriptional Profiling Identifies Functionally Distinct Human Dermal Fibroblast Subpopulations. *J. Invest. Dermatol.* **138**, 811–825 (2018).

93. Traag, V. A., Waltman, L. & van Eck, N. J. From Louvain to Leiden: guaranteeing well-connected communities. *Sci. Rep.* **9**, 5233 (2019).

94. Blondel, V. D., Guillaume, J.-L., Lambiotte, R. & Lefebvre, E. Fast unfolding of communities in large networks. *J. Stat. Mech.* **2008**, P10008 (2008).

95. Korsunsky, I. *et al.* Fast, sensitive and accurate integration of single-cell data with Harmony. *Nat. Methods* **16**, 1289–1296 (2019).

96. Li, B. *et al.* Cumulus provides cloud-based data analysis for large-scale single-cell and single-nucleus RNA-seq. *Nat. Methods* **17**, 793–798 (2020).

97. McInnes, L., Healy, J., Saul, N. & Großberger, L. UMAP: Uniform Manifold Approximation and Projection. *Journal of Open Source Software* **3**, 861 (2018).

98. Aliee, H. & Theis, F. J. AutoGeneS: Automatic gene selection using multi-objective optimization for RNA-seq deconvolution. *Cell Syst* **12**, 706–715.e4 (2021).

99. Wolf, F. A., Angerer, P. & Theis, F. J. SCANPY: large-scale single-cell gene expression data analysis. *Genome Biol.* **19**, 15 (2018).

100. Garcia-Alonso, L., Holland, C. H., Ibrahim, M. M., Turei, D. & Saez-Rodriguez, J. Benchmark and integration of resources for the estimation of human transcription factor activities. *Genome Res.* **29**, 1363–1375 (2019).

101. Holland, C. H. *et al.* Robustness and applicability of transcription factor and pathway analysis tools on single-cell RNA-seq data. *Genome Biol.* **21**, 36 (2020).

102. Sturm, G. *et al.* Scirpy: a Scanpy extension for analyzing single-cell T-cell receptor-sequencing data. *Bioinformatics* **36**, 4817–4818 (2020).

103. Heimberg, G. *et al.* A cell atlas foundation model for scalable search of similar human cells. *Nature* **638**, 1085–1094 (2025).

104. Efremova, M., Vento-Tormo, M., Teichmann, S. A. & Vento-Tormo, R. CellPhoneDB: inferring cell–cell communication from combined expression of multi-subunit ligand–receptor complexes. *Nat. Protoc.* **15**, 1484–1506 (2020).

105. Hirota, T. *et al.* Genome-wide association study identifies eight new susceptibility loci for atopic dermatitis in the Japanese population. *Nat. Genet.* **44**, 1222–1226 (2012).

106. Weidinger, S. *et al.* A genome-wide association study of atopic dermatitis identifies loci with overlapping effects on asthma and psoriasis. *Hum. Mol. Genet.* **22**, 4841–4856 (2013).

107. Baurecht, H. *et al.* Genome-wide comparative analysis of atopic dermatitis and psoriasis

gives insight into opposing genetic mechanisms. *Am. J. Hum. Genet.* **96**, 104–120 (2015).

108. Schaarschmidt, H. *et al.* A genome-wide association study reveals 2 new susceptibility loci for atopic dermatitis. *J. Allergy Clin. Immunol.* **136**, 802–806 (2015).

109. Paternoster, L. *et al.* Multi-ancestry genome-wide association study of 21,000 cases and 95,000 controls identifies new risk loci for atopic dermatitis. *Nat. Genet.* **47**, 1449–1456 (2015).

110. Kichaev, G. *et al.* Leveraging Polygenic Functional Enrichment to Improve GWAS Power. *Am. J. Hum. Genet.* **104**, 65–75 (2019).

111. Johansson, Å., Rask-Andersen, M., Karlsson, T. & Ek, W. E. Genome-wide association analysis of 350 000 Caucasians from the UK Biobank identifies novel loci for asthma, hay fever and eczema. *Hum. Mol. Genet.* **28**, 4022–4041 (2019).

Acknowledgements

We thank members of the Regev, Xavier and Geha laboratories for helpful discussions. We thank L. Gaffney, A. Hupalowska, H. Kang and S. Aldrich for help with figure preparation and E. Heppenheimer for critical reading of the manuscript. This research was supported by NHGRI grants 5RM1 HG006193 (Center for Cell Circuits, to A.R.), Klarman Cell Observatory (A.R., R.J.X), DK043351 and DK114784 (to R.J.X), NIAID/NIH grant 1UM1AI151958 (to R.S.G.), and a gift from the Food Allergy Science Initiative (to A.R. and R.J.X), a gift from the Manton Foundation (to A.R. and R.J.X), and HHMI (to A.R.). E.F. is supported by an EMBO Long-Term fellowship, J.M.L-C. by NIAID T32 grant (5T32AI007512-32), NIH award (UL1 TR002541) and a Dermatology Foundation Career Development Award. C.A.L. is supported by a Stanford Science Fellowship. A.R. was a Howard Hughes Medical Institute Investigator (until July 31, 2020). This paper is part of the Human Cell Atlas.

Author Contributions

E.F., G.E., O.R.-R., R.S.G., R.J.X. and A.R. conceived and designed the project. E.F. designed and performed experiments. E.F., G.E., O.A., T.J., J.D and T.M.D. analyzed and interpreted the data, with guidance from A.R. G.E. designed and led data analysis, with guidance from A.R. M.B.A-P. performed clinical work. C.A.L. contributed to data analysis. E.F., M.B.A-P, J.M.L-C. collected biopsies, E.P.F. and I.T.-S. performed additional tissue processing and scRNA-seq experiments. E.F., S.I. performed mouse MC903 experiments. M.S., J.W. and T.M.D. provided experimental assistance. H.C., S.K., H.L., B.L., A.C., B.W., W.P., L.S., C.P., and J.C. assisted in patient recruitment and biopsy collection. G.P.S., T.M.D., J.D., O.R.-R., R.S.G., R.J.X. and A.R. provided project oversight and acquired funding. E.F., G.E., O.A., T.J., T.M.D., R.J.X. and A.R. wrote the manuscript with input from all authors.

Competing Interests

A.R. was a founder and equity holder of Celsius Therapeutics, is an equity holder in Immunitas Therapeutics and until 31 July 2020 was an SAB member of Syros Pharmaceuticals, Neogene Therapeutics, Asimov and ThermoFisher Scientific. From 1 August 2020, A.R. is an employee of Genentech, a member of the Roche Group, with equity in Roche. R.J.X. is a co-founder of Celsius Therapeutics, Jnana Therapeutics and director of Moonlake Immunotherapeutics. R.J.X. is an SAB member of Magnet Biomedicine and of Nestle. From 19 October 2020 and 4 April 2022 respectively, O.R-R and G.E. are employees of Genentech, a member of the Roche Group, and have equity in Roche. The remaining authors declare no competing interests.

Figure legends

Figure 1. Multi-modal single-cell atlas of healthy, non-lesional and lesional skin of atopic dermatitis patients. a, Study overview. 13 lesional (11 from AD and 2 from scleroderma patients), 12 non-lesional (10 AD, 2 scleroderma), and 6 healthy biological samples; For AD, 32 channels were loaded (lesional AD, n = 17 channels; non-lesional, n = 15 channels. For scleroderma, 4 channels were loaded (lesional scleroderma, n = 2 channels; non-lesional scleroderma, n = 2 channels). For healthy controls, n = 7 channels were loaded. Created in BioRender. Kang, H. (2025) https://BioRender.com/qh3ziku. **b-f**, Skin cell atlas. Two-dimensional (2D) embedding of scRNA-seq profiles (dots) from all donors, colored by annotated coarse cell types (b), granular cell subsets (c), disease state (e), or z-scored expression values of epidermal inflammatory marker genes (f), along with distribution of their expression values across disease conditions (x-axis), white dot: median expression; ns: non-significant; two-sided Wald tests; **Benjamini–Hochberg FDR**. Lesional, n = 11 samples (54,267 cells), non-lesional, n = 10 samples (32,972 cells), healthy, n = 6 samples (28,321 cells). **d**, Mean z-scored expression values (color) of marker genes (rows) across 86 granular cell subsets (columns; color code as in **c**); Log(TP10K+1) corresponds to log-transformed UMIs per 10k. Top bar: coarse cell types (as in **b**). **g-i**, Increased immune cell proportions in lesional skin. **g**, Proportion (y-axis) of granular cell subsets (columns, ordered within broad categories (color bar) by proportion of cells from lesional samples) in healthy (green), non-lesional (blue) and lesional (orange) samples. Color tones: individual patients. Bottom: total number of cells for each subset in the dataset. **h-i**, Distribution of proportions of each coarse cell type that is significantly increased (h) or decreased (i) in lesions (*vs*. healthy controls) across healthy, non-lesional and lesional conditions. Lesional, n = 14 channels (9 samples), non-lesional, n = 12 channels (8 samples), healthy, n = 7 channels (6

samples). Center line: median; box limits: first and third quartiles; whiskers: 1.5× interquartile range. ns: non-significant; Dirichlet regression; two-sided Wald tests; Benjamini–Hochberg FDR across cell types; Dots: cell type proportion by channel.

Figure 2. Shift in keratinocyte differentiation in atopic dermatitis.

a-f, Full keratinocyte differentiation trajectory from basal to terminal cornified layer. **a,c**, 2D embedding and PAGA connectivity map (nodes and edges) of keratinocyte scRNA-seq profiles from all samples, colored by annotated keratinocyte cell subset (a) or by z-scored expression of keratinocyte subset marker genes (c). Arrow in **a**: differentiation axis. **b**, Mean expression (log(TP10K+1), node color) and proportion of expressing cells (node size) of marker genes (columns) of keratinocyte cell subset (rows). Arrow: keratinocyte differentiation axis. **d**, Scaled expression values of marker genes in cells (columns) from healthy controls ordered along diffusion pseudotime (DPT) of keratinocyte differentiation from basal to terminal cornified cells. Data were downsampled (**Methods**) to show equal numbers of cells for each subset. **e**, Immuno-histochemistry (IHC) derived from the Human Protein Atlas[89] of healthy skin tissue sections with subset markers. Dotted line: border between epidermis (top) and dermis (bottom). Scale bar: 200µm. **f-l**, Shift towards cornified KC1s in differentiation in lesional skin. **f-h**, Proportions of keratinocyte cell subsets in scRNA-seq. Lesional, n = 14 channels (9 samples), non-lesional, n = 12 channels (8 samples), healthy, n = 7 channels (6 samples). (f,h) or deconvolved (g, **Methods**) bulk RNA-seq data[19]. Center line: median; box limits: first and third quartiles; whiskers: 1.5× interquartile range. Dirichlet regression; two-sided Wald tests; Benjamini–Hochberg FDR across cell types. ns, non-significant; Dots: cell type proportions by channels (f,h) or samples (g) profiled in the specified disease status. **i**, Changes in keratinocyte proportions along differentiation. Changes in cell proportions in each cell type (red, increase; blue, decrease; scale bar, bottom). **j**,

Aberrant KC differentiation trajectories in AD skin. Distribution of DPT (**Methods**) for KC5 and cornified KC cells, colored by disease state. Mann–Whitney U test (two-sided, unpaired); P values were Benjamini–Hochberg FDR–adjusted across the tested cell types/contrasts. Vertical dashed lines: median. **k,l**, Scaled expression of differentially expressed genes that are decreased (**k**, top), increased (**k**, bottom) or are *IL-1* family genes (**l**) across DPT-ordered cells (columns) in lesional, non-lesional, or healthy skin. Arrows: keratinocyte differentiation axis. Data is downsampled (**Methods**). Color bars as in **d**. Colored arrows in **k,l**: increased (green) or decreased (red) expression in lesional skin.

Figure 3. Increase in *MMP12*$^{+}$ DCs and mmDCs in AD through an activation trajectory. **a,b**, Skin myeloid cells. **a**, 2D embedding of myeloid scRNA-seq profiles (dots), colored by cell subset. **b,** Mean (dot color) expression and fraction of expression cells (dot size) of myeloid cell markers (columns) across cell subsets (rows). **c-e**, Two trajectories of dendritic cell activation. **c**, 2D embedding of selected DC scRNA-seq profiles and directed PAGA connectivity map (nodes and edges) from all samples, colored by cell subset, DPT, or z-scored expression of marker genes. Dashed arrows: activation trajectories. **d,e**, Expression of marker genes in cells (columns) from all samples ordered by DPT of DC activation trajectory 1 (d) or 2 (e). Colored bars: DPT (top) and cell annotation (bottom, as in **c**). Data were down sampled (**Methods**) to show equal numbers of cells for each subset. **f,g**, Increased proportion of DC *MMP12*$^{+}$ and mmDC cells in lesional skin. Proportion of different DC cell subsets in scRNA-seq; Lesional, n = 14 channels (9 samples), non-lesional, n = 12 channels (8 samples), healthy, n = 7 channels (6 samples). (f) or deconvolved bulk RNA-seq[19] (g). Center line: median; box limits: first and third quartiles; whiskers: 1.5× interquartile range. Dirichlet regression. ns, non-significant; *Dots:* cell type proportion by channels

(f) or samples (g) profiled in the specified disease status. **h-k**, A *CCL22*^{hi} *CCL17*^{hi} *CCL19*^{lo} *IDO1*^{lo} state enriched in mmDC from AD skin. **h-j**, 2D embedding of mmDCs profiles from our data and 22 additional scRNA-seq studies (**Methods**) colored by condition (h), study (i), or marker gene expression (j). **k**, Mean expression and proportion of expressing cells of mmDC marker genes in mmDCs from AD or non-AD samples.

Figure 4. An *IL13/IL22/IL26* program in T cell clones expanded in AD.

a, 2D embedding of skin lymphocyte scRNA-seq profiles from all samples. **b**, Mean expression and percent of lymphocytes expressing marker genes by cell subset. **c**, 2D embedding of scRNA-seq profiles (as in **a**), colored by binarized expression of *IL13/IL22/IL26* topic 190 (**Methods**). **d**, Probability of top scoring genes from topic 190. **e**, Genes with highest correlation to *IL13*-expression across single lymphocyte profiles. **f,g**, Proportions of specific cell subsets across sample types. Lesional, n = 14 channels (9 samples), non-lesional, n = 12 channels (8 samples), healthy, n = 7 channels (6 samples) for (f, g T/ILC cell types); Lesional, n = 9 channels (6 samples), non-lesional, n = 8 channels (5 samples), healthy, n = 6 channels (5 samples) for (g - Plasma IgG cell types). Center line: median; box limits: first and third quartiles; whiskers: 1.5× interquartile range. p-values reported for f,k and FDR values reported for g. Dirichlet regression; two-sided Wald tests; Benjamini–Hochberg FDR across cell types. ns, non-significant; Dots: cell type proportion by channel. **h,i**, Mean expression and percent of cells expressing selected lesion-enriched genes in ILC subsets (h) or Tregs (i). **j**, Differential topic expression (colored by -$\log_{10}$(Benjamini–Hochberg (BH) FDR) ranked by t statistic. **k**, Proportion of lymphocytes expressing topic 190 or effector cytokines; Lesional, n = 17 channels (11 samples), non-lesional, n = 15 channels (10 samples), healthy, n = 7 channels (6 samples). FDR, Mann–Whitney U test

(Wilcoxon rank-sum; unpaired, two-sided). ns, non-significant; Dots: cell type proportion by channel. **l**, Fraction of single, double or triple positive *IL13/IL22/IL26* co-expressing cells in different conditions or lymphoid cell subset. **m**, Mean expression (min-max scaled log(TP10K+1), dot color) and percent of cells expressing *IFNG*, *IL13*, *IL22*, *IL26* across lymphocyte cell subsets. **n-p**, 2D embedding of CD4+ T cell 5'-scRNA-seq profiles from lesional skin of eight patients (*n*=6,047 cells) (**Methods**), colored by cell subset (n), clone size (o), z-scored expression of cytokines or z-scored scaled topic 190 score (p). **q**, Topic 190 score (mean of z-scored scaled scores in patients with expanded (≥2) and non-expanded (1) CD4+ T cells. Dots, patient samples. Center line: median; box limits: first and third quartiles; whiskers: 1.5× interquartile range. Welch's two-sided t-test. *n*=8 patient samples. Single-cell values were aggregated to sample means prior to testing. **r**, Fraction of single, double or triple positive co-expressing cells in non-expanded and expanded T cell clones expressing *IL13*. **s**, Effect size ($\log_2$(fold change)) and significance (-$\log_{10}$(FDR)) of differential gene expression in expanded *vs*. non-expanded $CD4^+$ T cells (**Methods**).

Figure 5. Increase in immunoregulatory fibroblasts in AD skin stroma.

a-c, Skin vascular endothelial cells. **a,b**, 2D embedding of vascular endothelial cell scRNA-seq profiles from all samples, colored by annotation (a), blood vessel type (b, left), or z-scored expression of vessel marker genes (b, right). **c**, Mean expression (dot color) and percent of expressing cells (dot size) of marker genes (columns) across vascular endothelial cell subsets (rows). **d-f**, Skin fibroblasts. **d**, 2D embedding of fibroblasts scRNA-seq profiles from all samples, colored by granular annotations. **e**, Mean expression (dot color) and percent of expressing cells (dot size) of marker genes (columns) across subsets (rows). **f**, *CCL19*$^+$ *IL4I1*$^+$ fibroblasts preferential express antigen presentation genes. Z-scored mean expression (color) of HLA class I

and II genes (columns) across fibroblast subsets (rows). BH FDR adjusted across genes within each group: ***<0.01, two-sided t-test. Exact P values are provided in the Source Data File. **g,h**, *CCL19*$^{+}$ *IL4I1*$^{+}$ fibroblasts increase in AD and activate an inflammatory expression program. **g**, Proportions (y axis) of stromal cell subsets (x axis) across conditions (bar color). Lesional, n = 14 channels (9 samples), non-lesional, n = 12 channels (8 samples), healthy, n = 7 channels (6 samples). Center line: median; box limits: first and third quartiles; whiskers: 1.5× interquartile range. ns: non-significant; Dirichlet regression; two-sided Wald tests; Benjamini–Hochberg FDR across cell types ($q < 0.10$). Dots: cell type proportion by channel. **h**, Z-scored mean expression of genes (columns) differentially expressed between disease conditions (rows) for stromal cell subsets (top).

Figure 6. Two multicellular communities associated with disease.

a, 2D embedding of healthy, non-lesional and lesional channels by the first two PCs derived from a PCA of cell composition, colored by disease status or scaled proportions (z-scores of centered log-ratio (CLR) transformed proportions) of indicated cell subsets. **b**, PC2 loading of cell subsets with top (red) and bottom (black) 15 loadings. **c**, Correlation coefficient (Spearman's ρ, colorbar) between proportions of each pair of cell subsets (rows, columns) across samples. Inset: a cluster of *IL13/IL22/IL26* T cells, mmDCs and *CCL19*$^{+}$ *IL4I1*$^{+}$ fibroblasts; red: cell subsets with high PC2 loading. **d,e**, Potential cell-cell interactions between mmDCs and *IL13/IL22/IL26* co-expressing T cells in lesional skin. Mean z-scored expression values of ligand or receptor genes specifically expressed in mmDCs (d, left, columns) or *IL13/IL22/IL26* T cells (e, left, columns) and their cognate interacting partners (right, rows) across all subsets (right, columns, **Methods**) with a significant interacting partner expression. Edges: ligand-receptor pairs with z-scored expression values greater than 1.0 in at least one cell subset. Red: cell subsets with high PC2 loadings. **f**,

Multiple positive feedback loops may initiate or stabilize multicellular communities and impact KCs. Cell subsets (nodes) connected from ligand-expressing to receptor expressing subset (edges) where proportion of the receptor-expressing subsets is correlated with ligand expression across samples (see also **Supplementary Fig. 13e**). Red: highly correlated pairs (Spearman's $\rho > 0.5$). **g**, A multicellular pathological circuit in AD lesional skin. Schematic showing a model of the interplay between aberrant KC differentiation from KC1 (bottom, epidermis) to cornified KC2 subsets (top, epidermis) and disease-associated multicellular communities with the core of community 1 including clonally expanded *IL13*$^{+}$/*IL22*$^{+}$/*IL26*$^{+}$ T cells, mmDCs, *CCL19*$^{+}$ *IL4I1*$^{+}$ fibroblasts and cycling ILCs as well as the community 2 core of *IL1B*$^{+}$ DCs, T *CREM*^{hi} and neutrophils. The intercellular feedback loops predicted to contribute to community formation are shown (green arrows) and negative impact of community 1 on terminal KC differentiation is indicated (red arrow). GWAS genes specifically enriched in each cell subsets are displayed (blue boxes).

Editorial Summary

In atopic dermatitis (AD), skin barrier disruption leads to chronic inflammation. Here, the authors use single-cell sequencing to map human skin, uncovering AD-specific cell states and populations involved in immune responses and cell differentiation.

Peer review information: *Nature Communications* thanks the anonymous reviewers for their contribution to the peer review of this work. A peer review file is available.

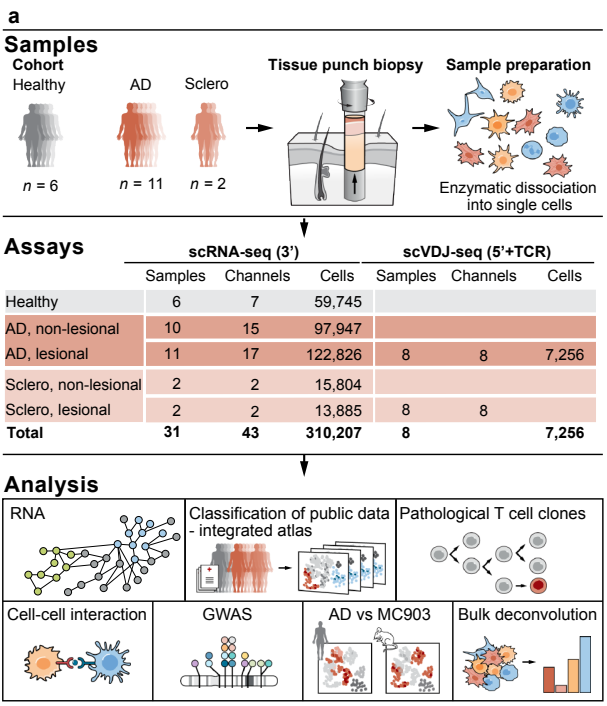
a
Samples
Cohort
Healthy
AD
Sclero
n = 6
n = 11
n = 2
Tissue punch biopsy
Sample preparation
Enzymatic dissociation into single cells
Assays
scRNA-seq (3')
scVDJ-seq (5'+TCR)
Samples Channels Cells Samples Channels Cells
Healthy 6 7 59,745
AD, non-lesional 10 15 97,947
AD, lesional 11 17 122,826 8 8 7,256
Sclero, non-lesional 2 2 15,804
Sclero, lesional 2 2 13,885 8 8
Total 31 43 310,207 8 7,256
Analysis
RNA
Classification of public data - integrated atlas
Pathological T cell clones
Cell-cell interaction
GWAS
AD vs MC903
Bulk deconvolution

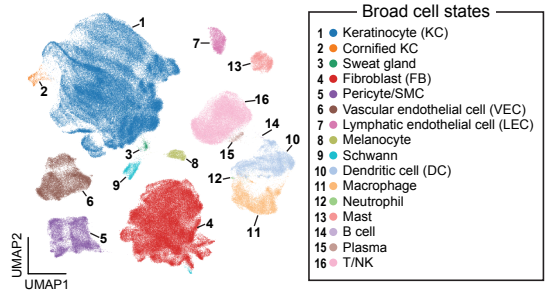
b
UMAP2
UMAP1
Broad cell states
1 Keratinocyte (KC)
2 Cornified KC
3 Sweat gland
4 Fibroblast (FB)
5 Pericyte/SMC
6 Vascular endothelial cell (VEC)
7 Lymphatic endothelial cell (LEC)
8 Melanocyte
9 Schwann
10 Dendritic cell (DC)
11 Macrophage
12 Neutrophil
13 Mast
14 B cell
15 Plasma
16 T/NK

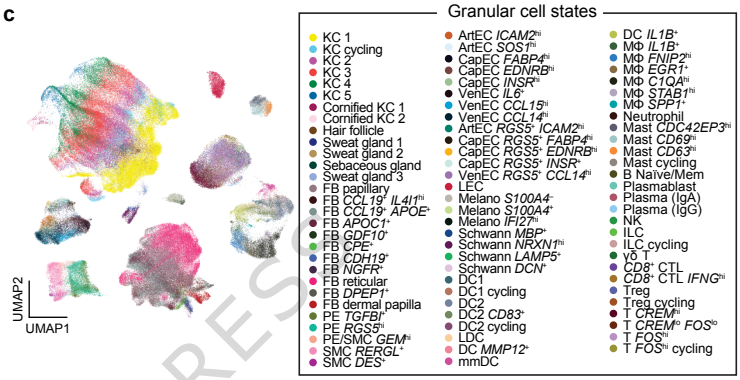
c
UMAP2
UMAP1
Granular cell states
KC 1
KC cycling
KC 2
KC 3
KC 4
KC 5
Cornified KC 1
Cornified KC 2
Hair follicle
Sweat gland 1
Sweat gland 2
Sebaceous gland
Sweat gland 3
FB papillary
FB CCL19hi IL4I1hi
FB CCL19hi APOEhi
FB APOC1hi
FB GDF10hi
FB CPEhi
FB CDH19hi
FB NGFRhi
FB reticular
FB DPEP1hi
FB dermal papilla
PE TGFBIhi
PE RGS5hi
PE/SMC GEMhi
SMC RERGLhi
SMC DEShi
ArtEC ICAM2hi
ArtEC SOS1hi
CapEC FABP4hi
CapEC EDNRBhi
CapEC INSRhi
VenEC IL6hi
VenEC CCL15hi
VenEC CCL14hi
ArtEC RGS5hi ICAM2hi
CapEC RGS5hi FABP4hi
CapEC RGS5hi EDNRBhi
CapEC RGS5hi INSRhi
VenEC RGS5hi CCL14hi
LEC
Melano S100A4lo
Melano S100A4hi
Melano IFI27hi
Schwann MBPhi
Schwann NRXN1hi
Schwann LAMP5hi
Schwann DCNhi
DC1
DC1 cycling
DC2
DC2 CD83hi
DC2 cycling
LDC
DC MMP12hi
mmDC
DC IL1Bhi
MΦ IL1Bhi
MΦ FNIP2hi
MΦ EGR1hi
MΦ C1QAhi
MΦ STAB1hi
MΦ SPP1hi
Neutrophil
Mast CDC42EP3hi
Mast CD69hi
Mast CD63hi
Mast cycling
B Naïve/Mem
Plasmablast
Plasma (IgA)
Plasma (IgG)
NK
ILC
ILC cycling
γδ T
CD8hi CTL
CD8hi CTL IFNGhi
Treg
Treg cycling
T CREMhi
T CREMlo FOSlo
T FOShi
T FOShi cycling

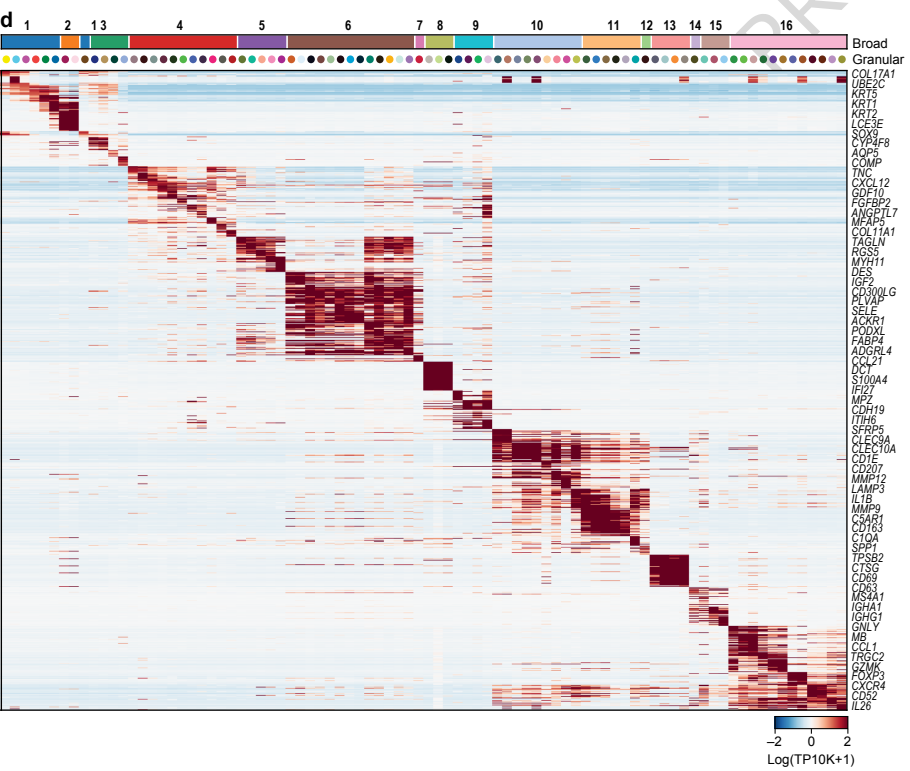
d
Broad
Granular
Log(TP10K+1) mean z-score

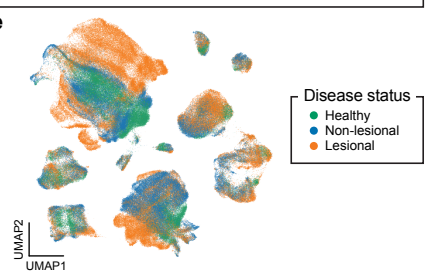
e
UMAP2
UMAP1
Disease status
Healthy
Non-lesional
Lesional

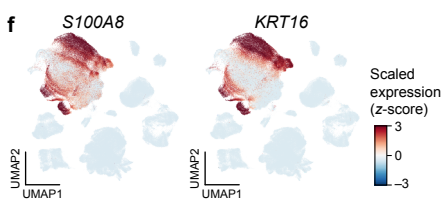
f
S100A8
KRT16
UMAP2
UMAP1
Scaled expression (z-score)

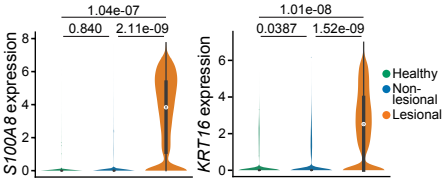
1.04e-07
0.840
2.11e-09
1.01e-08
0.0387
1.52e-09
S100A8 expression
KRT16 expression
Healthy
Non-lesional
Lesional

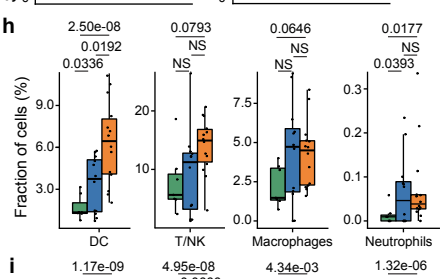
h
2.50e-08
0.0192
0.0336
0.0793
NS
0.0646
NS
NS
0.0177
NS
0.0393
Fraction of cells (%)
DC
T/NK
Macrophages
Neutrophils

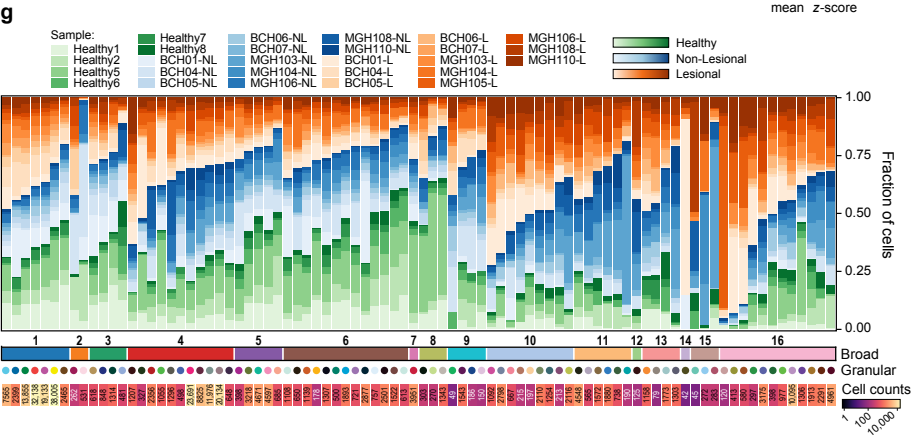
g
Sample:
Healthy1
Healthy2
Healthy5
Healthy6
Healthy7
Healthy8
BCH01-NL
BCH04-NL
BCH05-NL
BCH06-NL
BCH07-NL
MGH103-NL
MGH104-NL
MGH106-NL
MGH108-NL
MGH110-NL
BCH01-L
BCH04-L
BCH05-L
BCH06-L
BCH07-L
MGH103-L
MGH104-L
MGH105-L
MGH106-L
MGH108-L
MGH110-L
Healthy
Non-Lesional
Lesional
Fraction of cells
Broad
Granular
Cell counts

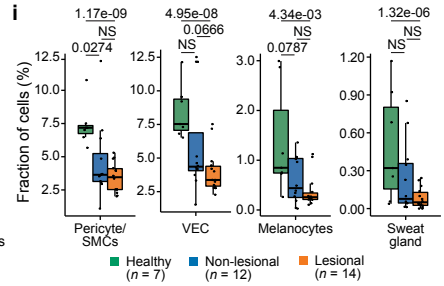
i
1.17e-09
NS
0.0274
4.95e-08
0.0666
NS
4.34e-03
NS
0.0787
1.32e-06
NS
Fraction of cells (%)
Pericyte/ SMCs
VEC
Melanocytes
Sweat gland
Healthy (n = 7)
Non-lesional (n = 12)
Lesional (n = 14)

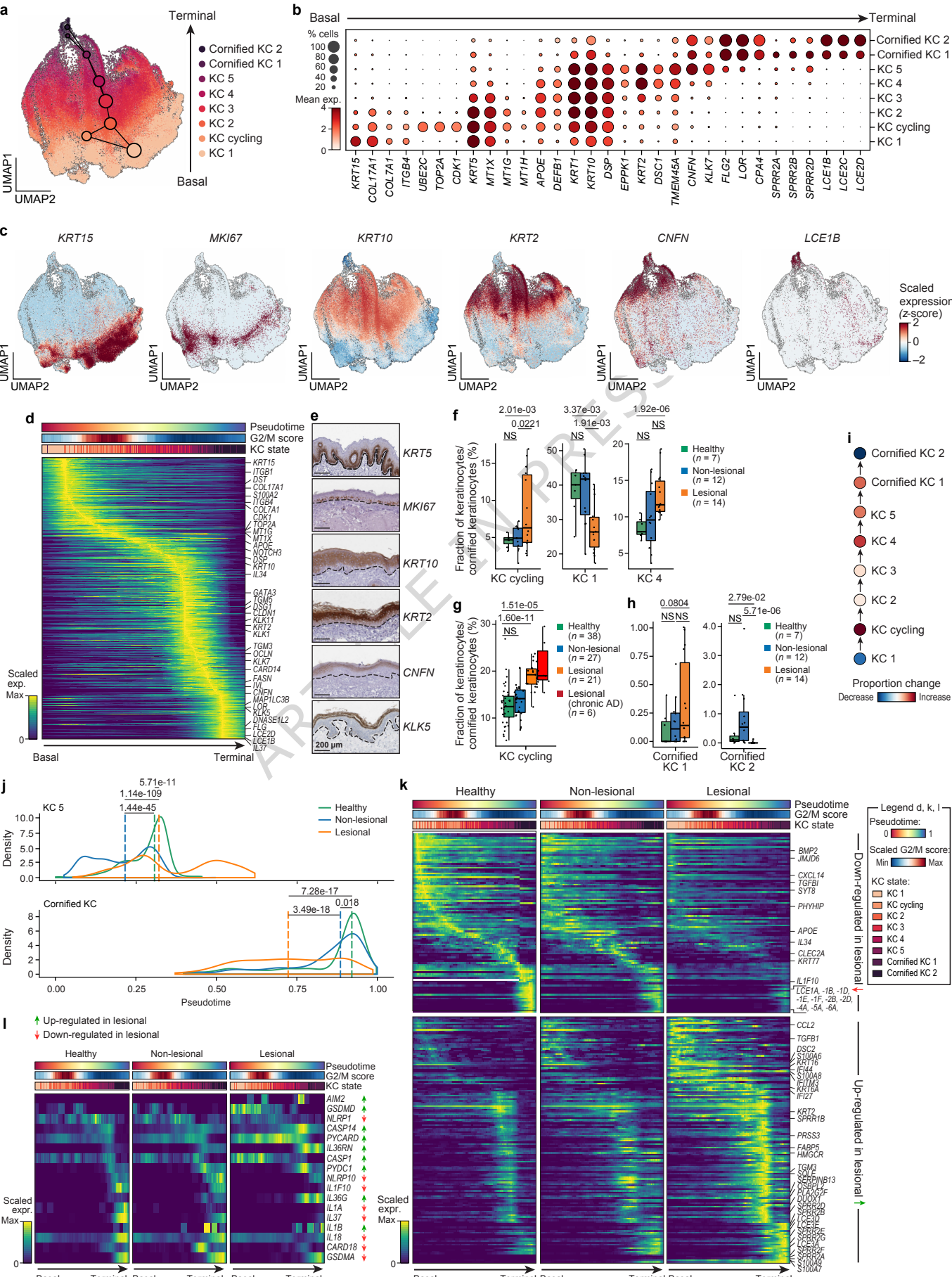
a
Terminal
Basal
Cornified KC 2
Cornified KC 1
KC 5
KC 4
KC 3
KC 2
KC cycling
KC 1
UMAP1
UMAP2
b
Basal
Terminal
% cells
Mean exp.
KRT15 COL17A1 COL7A1 ITGB4 UBE2C TOP2A CDK1 KRT5 MT1X MT1G MT1H APOE DEFB1 KRT1 KRT10 DSP EPPK1 KRT2 DSC1 TMEM45A CNFN KLK7 FLG2 LOR CPA4 SPRR2A SPRR2B SPRR2D LCE1B LCE2C LCE2D
c
KRT15
MKI67
KRT10
KRT2
CNFN
LCE1B
Scaled expression (z-score)
d
Pseudotime
G2/M score
KC state
Scaled exp.
Basal
Terminal
e
KRT5
MKI67
KRT10
KRT2
CNFN
KLK5
200 µm
f
Fraction of keratinocytes/ cornified keratinocytes (%)
KC cycling
KC 1
KC 4
Healthy (n = 7)
Non-lesional (n = 12)
Lesional (n = 14)
g
Fraction of keratinocytes/ cornified keratinocytes (%)
KC cycling
Healthy (n = 38)
Non-lesional (n = 27)
Lesional (n = 21)
Lesional (chronic AD) (n = 6)
h
Cornified KC 1
Cornified KC 2
Healthy (n = 7)
Non-lesional (n = 12)
Lesional (n = 14)
i
Cornified KC 2
Cornified KC 1
KC 5
KC 4
KC 3
KC 2
KC cycling
KC 1
Proportion change
Decrease
Increase
j
KC 5
Cornified KC
Density
Pseudotime
Healthy
Non-lesional
Lesional
k
Healthy
Non-lesional
Lesional
Pseudotime
G2/M score
KC state
Down-regulated in lesional
Up-regulated in lesional
Legend d, k, l
Pseudotime:
Scaled G2/M score:
KC state:
KC 1
KC cycling
KC 2
KC 3
KC 4
KC 5
Cornified KC 1
Cornified KC 2
l
Up-regulated in lesional
Down-regulated in lesional
Healthy
Non-lesional
Lesional
Pseudotime
G2/M score
KC state
AIM2 GSDMD NLRP1 CASP14 PYCARD IL36RN CASP1 PYDC1 NLRP10 IL1F10 IL36G IL1A IL37 IL1B IL18 CARD18 GSDMA
Scaled expr.
Basal
Terminal